University of Salerno
Department of Physics "E. R. Caianiello" and Department of Mathematics

in consortium with

University of Campania "Luigi Vanvitelli"
Department of Mathematics and Physics

Doctoral School "Mathematics, Physics and Applications"
XXIX cycle
Curriculum Complex Systems

Thesis

The role of randomness in avalanche statistics and synchronization of spring-block models

Candidate
Valentina Esposito

Tutor
Dr. Eugenio Lippiello

Ph.D. Coordinator
Prof. Sandro Pace

Abstract

Spring-block models are the most simple description of a seismic fault reproducing at qualitative level experimental observations as the Gutenberg-Richter law. In the cellular automata version, the so-called OFC model, randomness is present only in the initial condition and avalanche sizes follow a power law distribution with an exponent depending on the dissipation parameter. The OFC model can be mapped in the evolution of a driven elastic interface in a disordered medium after adding randomness in the level of friction instability. In this case the avalanche size distribution is still a power law but with a stable exponent independent of the dissipation parameter. In the Thesis we study the mechanism responsible for the observed differences between the pure and the random OFC model, focusing on the role of synchronization leading to quasi-periodic behavior. In order to achieve a better understanding of synchronization and dissipation in the system we also study simplified models including mean-field models up to two-block systems. The role of relaxation is also discussed in these simplified systems.

Contents

Introduction **8**

1 Statistical features of seismic events **13**

1.1 Physical observables 13

1.1.1 Earthquake size 14

1.1.2 Scaling relationships 15

1.2 Distribution in size: Gutenberg-Richter Law 16

1.3 Distribution in time: Omori Law 18

1.4 Productivity Law 20

1.5 Earthquake spatial distribution 20

2 Statistical models: from spring-block model to self organized criticality **23**

2.1 The Burridge-Knopoff Model 23

2.2 Cellular Automata approach: Olami-Feder-Christensen Model . . . 25

2.3 Self Organized Criticality 29

2.3.1 Sandpile model 31

2.3.2 The generalized BTW model 32

3 The role of randomness in the SOC behavior of the models **37**

3.1 Elastic interfaces driven in a random medium: the depinning transition 37

3.1.1 The depinning transition with constant driving force 39

3.1.2 The depinning transition with elastic driving force 41

3.2 Mapping the elastic interfaces model on a cellular automaton one: the OFC* model . . . 44
3.2.1 The modified OFC* model . . . 48

4 The role of visco-elasticity in the SOC behavior of the models 51
4.1 Viscous coupling . . . 51
4.2 Viscous coupling in the OFC model: the OFCR model . . . 52
4.3 Viscous coupling in elastic interfaces model . . . 56

5 Mean Field analysis of the OFC and OFC* model 61
5.1 Fully connected model . . . 62
5.1.1 Synchronization mechanism . . . 64
5.2 Fixed Threshold and Jump to Zero . . . 65
5.2.1 Synchronization . . . 65
5.3 Uniform Threshold and Fixed Jump . . . 67
5.3.1 Synchronization . . . 67
5.3.2 Size distribution and percolative analysis of the distribution of the gaps . . . 70
5.3.3 Map to the Problem of First-Crossing . . . 72
5.4 Fixed Threshold and Random Jump . . . 74
5.4.1 Synchronization . . . 74
5.4.2 Size distribution . . . 74
5.4.3 Map to the problem of first crossing . . . 76
5.5 Random Threshold and Random Jump . . . 78
5.6 Mean field approach to the elastic interfaces problem . . . 79

6 Relaxation and the two blocks model: an analytical study 83
6.1 The model . . . 84
6.2 Jump to zero case: the periodic attractor . . . 85
6.3 Tang and Middleton: inhomogeneities and synchronization . . . 86
6.4 Relaxation and partial synchronization . . . 88
6.4.1 Partial Synchronization: $\epsilon < (1-\alpha)/2$ . . . 91
6.4.2 Synchronization: $(1-\alpha)/2 < \epsilon < (1-\alpha^2)/2\alpha$ . . . 94
6.4.3 Periodicity: $\epsilon > (1-\alpha^2)/2\alpha$ . . . 95

Conclusions **98**

Bibliography **103**

Introduction

Dynamics of the Earth crust depends on several mutually dependent mechanisms acting at different spatial and temporal scales. The interplay of these mechanisms produces instabilities in the stress field, leading to abrupt energy releases, i.e., earthquakes. Collective behavior in stress transfer and relaxation within the Earth crust leads to emergent properties described by stable phenomenological laws for a population of many earthquakes in size, time and space domains. This observation has stimulated a statistical mechanics approach to earthquake occurrence, applying ideas and methods, as scaling laws, universality, fractal dimension, renormalization group, to characterize the physics of earthquakes.

A classical model for earthquake occurrence is the Burridge Knopoff (BK) spring-block model [1], where the fault between two tectonic plates is described as a lattice of rigid blocks elastically connected among them and driven onto a rough surface. Due to the relative movement of the tectonic plates, the stress on all the blocks increases until the stress of one block reaches an upper threshold, correspondent to the static friction, and relaxes, causing the slipping of the block and a rearrangement of the constraints on the neighboring blocks. This can possibly push other blocks to relax and trigger an avalanche of slippings, i.e., an earthquake. This model implements a separation of time scales, the one of the avalanches instantaneous respect to the one of the driving plate and it leads to a stick-slip dynamics. The model has attracted the interest of the physical community because of its ability to generate sequences of events following a power law in the size distribution. This feature is in agreement with the Gutenberg-Richter law [3] which describes the distribution of earthquake magnitudes in instrumental seismic catalogs. More precisely, in instrumental data sets the distribution of earthquake sizes is a power law with an exponent $\tau \simeq 1 + 2/3$. More generally,

the BK model is an interesting example of a self-organized critical system. Self-organized criticality (SOC) is a collective behavior whose main feature is that the dynamical system moves towards a critical point with scale invariance, without any tuning of adjustable external parameters. The most famous example of SOC is the sandpile model, introduced in 1987 by Bak, Tang and Wiesenfeld (BTW) [4]. Other examples are variants of this first model, like the forest fire model, a model for front propagation, evolution models for species, and so on [5]. A variant of great interest for the seismological community is the Olami Feder Christensen (OFC) model [2], a cellular automaton version of the BK model. Unlike the original BTW model, the OFC model is dissipative, because only a fraction of the stress released by the unstable site is redistributed to the neighbors. The size distribution in the OFC model is a power law with an exponent τ depending on the dissipation parameter α and in particular $\tau \simeq 1 + 2/3$ in a given range of α values.

The OFC model is very sensitive to small modifications of the toppling dynamics; for example, another implementation of the OFC model (the generalized BTW model [6]), where the unstable site's stress does not drop to zero, but drops of a fixed amount, leads to a stability of the exponent, since only the cut-off of the distribution depends on the dissipation. The introduction of randomness (OFC* model [7]) leads to the stability of the exponent as well, but interestingly in this latter case it is possible to map the model onto another well studied model, the elastic interface driven in a random media [8], which was initially developed to describe the evolution of interfaces between magnetic domains. This model describes the depinning transition, which is a phase transition between a pinned phase, where the interface is blocked, and a depinned phase, where the interface moves. In the case of elastic drive, we retrieve the same behavior of the avalanche statistics as in the OFC* model.

Nevertheless, the exponent τ of the OFC* model is significantly smaller than $\tau = 1 + 2/3$; moreover it is not possible to retrieve other statistical features, like the power law decay of the aftershock number, i.e. the Omori law [9]. The introduction of a relaxation mechanism, in a time scale in between the small one of the avalanches and the big one of the drive, leads to the presence of the aftershocks phenomenon. Also this model can be mapped onto a discretized one, the OFCR

model [7]. Interestingly, the introduction of a relaxation leads to a power law in the size distribution with a stable exponent $\tau \simeq 1 + 2/3$ independently of α.

The aim of this thesis is to study the mechanism responsible for the observed differences between the pure OFC model and the random OFC* model. More precisely we focus on the synchronization of individual blocks with each other, where by synchronization here we mean the possibility, for one block j, to partecipate to the same avalanche started by a block i, because of the stress rearrangement due to the instabilities. Middleton and Tang [11], indeed, observed that the OFC model with periodic boundary condition has a continuous set of neutrally stable periodic states. They found that inhomogeneity destroys these periodic states and causes synchronization, which is the building block for long range correlations. In particular, a change to open boundaries results in the invasion of the interior by a self-organized region, leading to a partially but non totally synchronized state. This mechanism for the self-organization appears to be related to the synchronization of the individual elements with each other and is proposed to explain the dependence of τ on the conservation parameter α. We therefore have investigated how the presence of randomness, as well as, of a relaxation mechanism affects synchronization in these systems.

In particular, in order to achieve a better understanding of how randomness affects the behavior of the exponent with dissipation, we decided then to consider how synchronization changes in the different cases.

We analyze, in mean field, several modifications of the original OFC model to study the role of randomness in synchronization and criticality of the system, varying the dissipation. Interestingly we found that in mean-field, unlike the 2-dim case, the OFC* and the generalized BTW belongs to the same universality class. Moreover we found that the standard OFC model in mean field displays an annealing of the synchronization mechanism that leads to criticality. These results are consistent with the claim, by Middleton and Tang, that the propagation of inhomogeneities from the boundaries is the main responsible of the partial synchronization, and then criticality, of the 2-dim original OFC model. Finally we implemented the viscosity in a simple model of two blocks under the original OFC dynamics, to understand how the relaxation mechanism of the OFCR model influences the synchronization. Since the simplicity of the model, it was

possible to perform an analytical study, and we found three different regimes of synchronization varying the relaxation parameter with the dissipation one.

The structure of the Thesis is the following: in Chapter 1 we introduce the physical observables involved in the earthquakes physics, and the empirical laws for earthquakes distribution in magnitude (GR law), in time (Omori Law) and in space, with the purpose to give a physical framework to our study; in Chapter 2 we introduce the BK model, the OFC model and the connection with self organized criticality; we also discuss the generalized BTW model; in Chapter 3 we introduce randomness in the models, and the mapping with the problem of the elastic interface driven in random media; in Chapter 4 we examine how the addition of viscosity effects changes the behavior of the models discussed. In Chapter 5 and 6 is presented our work: in Chapter 5 we perform a mean field analysis of the OFC models and its variations, while in Chapter 6 we report our analytical study of the two-blocks OFC model with relaxation.

Chapter 1

Statistical features of seismic events

In this Chapter we give an overview of the seismic context in which the model we study can be applied. The aim is to present the physical observables and the empirical statistical feature we will refer to in the rest of the Thesis.

1.1 Physical observables

Earthquake occurrence is the most striking evidence for the earth's crust not being a static object, but exposed to permanent deformation.

From a simplified point of view, the lithosphere is subdivided into several plates, which can move, mainly driven by thermal convection in the earth's mantle. The tectonic drift generates huge stresses at the plate boundaries and across the fractured areas in brittle regions of the lithosphere. These fractures, i.e., the *faults*, are organized into a complex network of planes without a characteristic size. Friction locks the free sliding causing the storage of high stresses along the fault plane. When the accumulated stress locally overcomes friction, both sides of the fault suddenly slip, generating an earthquake. The slipping of the fault is generally not homogeneous and not isotropic. Sliding initiates at a point (the earthquake hypocenter) and a slip front propagates outwards until friction locks again the two fault sides. This phenomenon is known as faulting. As a consequence, the slip is a

function of space and time, $\vec{D}(r,t)$, describing the actual sliding on the fault. The elastic energy stored on the fault is released as heat and seismic waves propagating in the system over very long distances.

1.1.1 Earthquake size

While early measures of earthquake sizes were based on the damage caused by an earthquake (Mercalli, 1902) [21], the first quantitative measure of the size of an earthquake was the *magnitude* m_L, introduced by the seismologist C. F. Richter (1930) [22] and linked to the logarithm of the seismic wave amplitudes. Richter's setup was based on a particular type of seismometer (Wood Anderson), placed at a distance of 100 km from the earthquake source. So different setups' measurements need corrections, depending on the location of the seismometer with respect to the source, the types of waves considered, and the geological settings.

A new scale was developed in the 1970s by Kanamori [23] to succeed the Richter magnitude scale (M_L), the Moment Magnitude Scale m_w:

$$m_w = \frac{2}{3}(\log_{10} M_0 - 9,1) \tag{1.1}$$

where M_0 is the *scalar seismic moment* at the hypocenter. Let us for simplicity assume a planar fault where the locations along the fault plane are characterized by two-dimensional vectors $\vec{x}$. Then, a slip vector $\vec{D}(\vec{x})$ can be assigned to each point of the fault plane, which describes the relative displacement of the material at both sides of the fault. The set of points where $\vec{D}(\vec{x}) \neq 0$ is called *rupture area*; let A denote its size. The seismic moment is defined by:

$$M_0 = \mu_0 \left| \int \vec{D}(\vec{x}) dx_1 dx_2 \right|.$$

Here μ_0 is the rigidity modulus of the lithosphere. If we introduce the mean displacement along the fault area:

$$\overline{D} = \frac{\mu_0 \left| \int \vec{D}(\vec{x}) dx_1 dx_2 \right|}{A},$$

we can rewrite the definition of the seismic moment as:

$$M_0 = \mu_0 A \overline{D}. \tag{1.2}$$

1.1.2 Scaling relationships

Experimental results have shown that the seismic moment scales with the rupture area as $M_0 \propto A^{\frac{3}{2}}$ [24]; assuming that the typical lengths along the direction parallel and perpendicular to the slip both scale with the same characteristic length L, we have $A = L^2$, and this leads to:

$$M_0 \propto L^3. \tag{1.3}$$

On the other hand, if we consider the relationship between the stress drop $\Delta\sigma$ due to the slip and the average strain $\overline{D}/L$:

$$\Delta\sigma \propto \mu_0 \frac{\overline{D}}{L} \tag{1.4}$$

we obtain:

$$M_0 \propto \Delta\sigma L^3. \tag{1.5}$$

For Eq.1.5 being consistent with Eq.1.3, the average displacement has to vary linearly with L, leading to a constant stress drop $\Delta\sigma$.

Another interesting consequence of the scaling isotropy concerns the energy released during the earthquake. As a first approximation, the energy of an earthquake with average slip $\overline{D}$ over an area A reads:

$$E \sim \frac{1}{2}\Delta\sigma \overline{D} A, \tag{1.6}$$

corresponding to the variation of the elastic energy stored in the fault. Confronting Eq.1.6 with the previous results we obtain:

$$E \sim \Delta\sigma L^3 \sim M_0.$$

One final remark comes from relating the magnitude with these scaling relationships, substituting Eq.1.3 in Eq.1.1; we obtain for the fault characteristic length

L:

$$L \propto 10^{0.5m}. \tag{1.7}$$

1.2 Distribution in size: Gutenberg-Richter Law

Now that we have defined the size of an earthquake in terms of magnitude, we introduce a very important scaling law that concerns the statistical properties of earthquakes, the Gutenberg-Richter law (1944) [25] [3], which relates the magnitude of earthquakes to their frequency. The law states that in any region, during a given period, the number $N(m)$ of earthquakes with magnitude larger then m is:

$$\log_{10}(N(m)) = a - bm \tag{1.8}$$

where b is the Gutenberg-Richter (GR) value and a is a constant that depends on the region and time considered, which indicates the overall degree of seismicity.

When plotting $\log_{10}(N(M)) = a - bM$ for actual data, it can be observed that the constant slope of the relationship generally fails at the largest and smallest magnitude events considered. At the lower end of the magnitude range it will be commonly observed to be flatter. This is generally attributed to the detection threshold of the particular seismic network that is monitoring the region. Earthquake catalogs are thus generally incomplete at the lowest magnitudes of sensitivity, resulting in a flattening of the curve. The magnitude of completeness m_c is defined, then, as the lower bound of the validity range of the GR law [26] (See Fig.1.1). Earthquake catalogs are also generally incomplete for the largest earthquakes recorded but for a different reason: the recording period is insufficient or too short to capture the occurrence of the largest earthquakes possible in the region.

Considering the logarithmic dependence of the magnitude on the seismic moment, and the linear relationship between the seismic moment and the energy, we obtain a power law distribution for the energy released:

$$P(E) \propto E^{-\beta}, \tag{1.9}$$

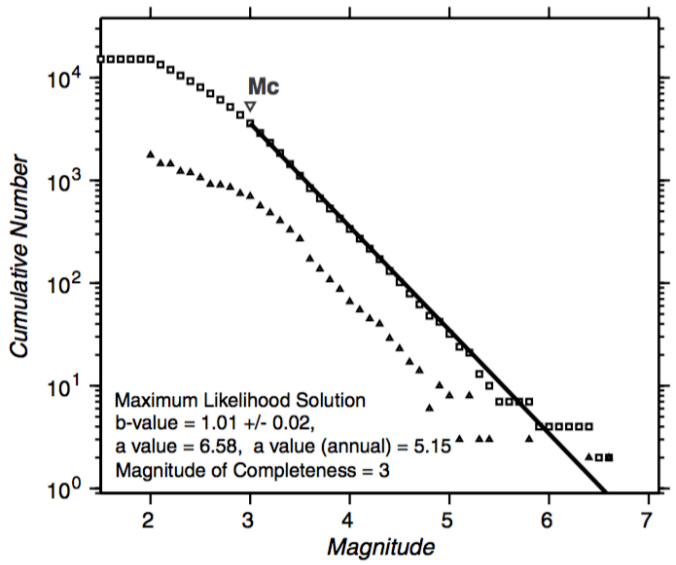

Figure 1.1: Earthquake statistics in Southern California for the time period 1954-1980 (adapted from [27]).

where

$$\beta = 1 + \frac{2}{3}b$$

The exponent b, in first approximation, is quite independent on the region or the time we are considering, and for tectonic earthquakes experimental data suggest a value $b \simeq 1$. Actually more recent studies have shown a dependence of the exponent on:

- different sub-regions in the same seismic catalogue [28];

- depth of the hypocenter [29];

- focal mechanism, in particular the rake angle λ, which characterizes the direction of slip on the fault plane [30] and can be related to the local level of differential stress [31] (as a consequence, some studies have suggested that the b-value can be used as a stress indicator, with lower b-values often associated with higher stresses [30]);

- magnitude range considered [32].

In all these studies fluctuations are about 20% of the b-value, at most, so it makes sense to consider the GR law with the exponent $b \simeq 1$, in first approximation, a robust feature of the statistical properties of the earthquakes occurrence.

1.3 Distribution in time: Omori Law

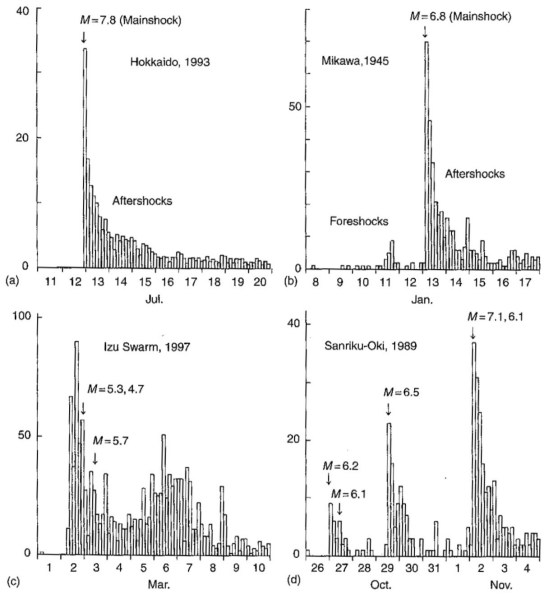

Figure 1.2: Examples of earthquake sequences: (a) mainshock-aftershock; (b) foreshock-mainshock-aftershock; (c) swarm (earthquake sequences without a clear mainshock); (d) successive occurrence of mainshock-aftershock sequences (adapted from [33]).

Considering now the earthquake distribution over time (in Fig.1.2 we report some examples), we define as *mainshock* the largest one in the sequence. Sometimes the mainshock is preceded by quiescence, other times by smaller magnitude

earthquake close in time to the mainshock, called *foreshocks*; in both cases, though, the mainshock is followed by smaller earthquakes within certain spatial and temporal windows, called *aftershocks*. They typically occur on or near the rupture plane of the mainshock, resulting from changes of stress and frictional properties of the fault zone caused by the mainshock.

It was first recognized by Omori (1894) [9] that the frequency of aftershocks is an hyperbolic decaying function of time. Later modified by Utsu (1961) [34], the Omori's law states that the aftershocks' occurrence rate decreases in time as:

$$n(t) = \frac{K}{(c+t)^p} \tag{1.10}$$

where $n(t)$ is the number of aftershocks at time t since the mainshock, K and c are empirical constants controlling, respectively, the total number of aftershocks and the onset of the power law decay. The value of p is typically close to 1 [35]. The values of these constants are obtained by data fitting for each aftershock sequence. It has been observed that the largest aftershock is usually about 1 magnitude unit smaller than the mainshock, independent of the mainshock magnitude. This is known as Bath's law [36]. However, because the data selection is retrospective and subjective, the size of aftershocks can vary substantially for different earthquake sequences.

The identification of a mainshock and its subsequent aftershocks is not a simple task for small mainshock sizes, because of the difficulty in separating triggered from spontaneous background events. In this case it is necessary to apply declustering methods able to perform such discrimination. Among several attempts based on spatial and temporal constraints for the aftershock, a simple approach consists in identifying as mainshocks all events separated in time and space from larger earthquakes. Aftershocks are all subsequent events occurring within a circular region of a given radius R centered at the main shock epicenter [47] [37].

The observation of a finite c is usually interpreted as a consequence of catalog incompleteness at the beginning of the aftershock sequence: immediately after a large earthquake, many aftershocks are not recorded in the catalog since either they are hidden in the mainshock coda wave, or they are skipped by the automatic event identification due to the overload of the apparatus [38] [39]. Analyses of

experimental sequences show that c depends on the mainshock magnitude m_M; this can be interpreted within a dynamical scaling framework [40]. Moreover, a dependence on the fault geometry, similar to the one found for the b value in the GR law, has been also measured for the c value [41].

1.4 Productivity Law

Another empirical feature of the aftershocks is the so-called productivity law, that states that the larger the mainshock magnitude, the larger is the total number of aftershocks belonging to the sequence. In particular the number of aftershocks n_{AS} belonging to a sequence increases exponentially with the mainshock magnitude m_M:

$$n_{AS} \propto 10^{\alpha m_M}$$

The α value obtained from data is about 0.8, slightly changing with the radius of the declustering procedure ($\alpha \in [0.72, 0.81]$ [42]). The result $\alpha \simeq 0.8$, also measured by a different method for aftershock identification based on networks of correlated events [43], is probably underestimated. Indeed, the evaluation of the number of aftershocks in sequences triggered by smaller mainshocks has a larger probability to include also events belonging to background activity and not triggered by the main event.

Other values for α have been obtained from different declustering methods. In particular, an estimation by the maximum likelihood of the epidemic type aftershock sequence (ETAS) model parameters usually leads to smaller values of α [44]. As a final remark, the relation between α and the b value in the GR law is important to discriminate if the triggering process is dominated by the small or the large events.

1.5 Earthquake spatial distribution

Experimental results [45] indicate that the spatial extent of aftershock activity, immediately after the mainshock (hours or days), is consistent with the dimension of the fault area fractured by the mainshock. According to Eq.1.7, therefore, one

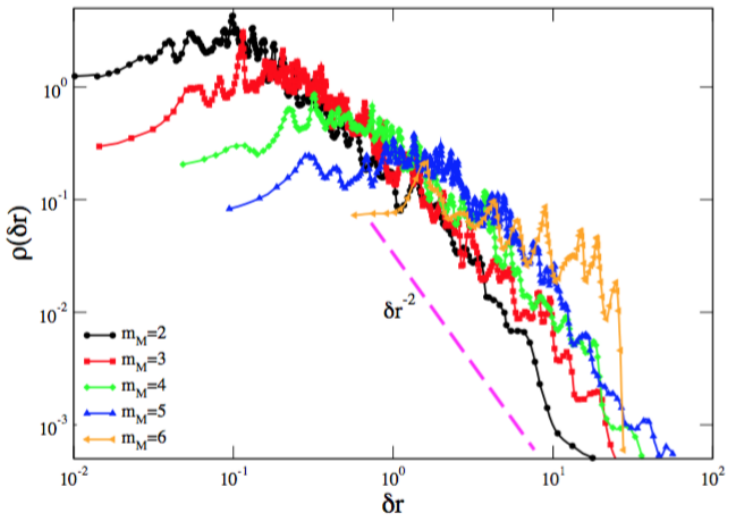

Figure 1.3: The spatial distribution of the aftershocks as a function of the epicentral distance δr, for different mainshock magnitudes m_M. The pink dashed line represents the power law decay $\rho(\delta r) \sim \delta r^{-2}$ (adapted from [54]).

expects that also the size of the aftershock area exponentially depends on the mainshock magnitude:

$$L(m) \propto 10^{\gamma m},$$

with $\gamma \propto 0.5$. This property can be recovered from the behavior of the distribution of distances between the hypocenters of each aftershock and its triggering mainshock. Usually, since the localization of earthquake depths presents a large uncertainty (sometimes as large as 1 km), many studies focus on the distribution $\rho(\delta r)$ of distances between epicenters. The quantity $\rho(\delta r)$ corresponds to the number of the aftershocks occurring at distance δr from the mainshock epicenter, divided for the total number of aftershocks. In Fig.1.3 we report this distribution for different values of the mainshock magnitude. The declustering method adopted to distinguish mainshocks and aftershocks is reported in [46]. As you may see, the smaller is the mainshock magnitude, the larger is the percentage of aftershocks happening at small δr.

The asymptotic decay of $\rho(\delta r)$ is consistent with a power law $\rho(\delta r) \sim \delta r^{-\nu}$. The determination of the exponent ν can give insights of the mechanism that triggers

the aftershock [47]. In fact, elastodynamics indicates that the displacement at a distance δr from a seismic source is composed by two contributions: a static one, usually defined as near field contribution, that decays as δr^{-2}, and a dynamic one, the far-field contribution caused by the transient passage of seismic waves, which exhibits a slower decay in space δr^{-1}. Aftershocks are mainly observed in the near-field where mainshocks have increased the difference between the shear and the normal stress, i.e. the static stress. However they also happen in regions of reduced static stress as well as at distances of several fault lengths from the mainshock [48]. In this case, far-field dynamic stress is the most reasonable cause for this remote triggering. The exponent ν allows to discriminate between triggering by static or dynamic stress.

Chapter 2

Statistical models: from spring-block model to self organized criticality

In this Chapter we introduce the spring-block model of the fault and its discrete version, the OFC model. We also report numerical results for the generalized BTW model, as a reference for a confrontation of these 2-dim models with our results in mean field.

2.1 The Burridge-Knopoff Model

In order to understand earthquake dynamics, we must first come back to the basics of fault mechanics. Burridge and Knopoff (1967) [1] introduced a simplified model for a single fault, capable of explaining the stick-slip dynamics of the earthquake. In this *spring-block* model, the fault is represented by two layers: for simplicity, one side of the fault is replaced with a rigid plate, the other side with an array of blocks that sticks to the plate because of static friction. To take into account a simplified elastic behavior of the rock, blocks are connected by springs among each other. The permanent driving due to tectonic forces is provided by elastic coupling of the blocks with the plate, which is assumed to move at a constant velocity. In figure 2.1 we report a one-dimensional example.

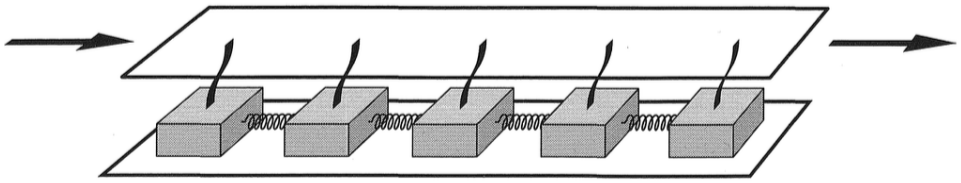

Figure 2.1: One-dimensional representation of a spring-block model (adapted from [49])

Indicating with $\vec{h}_i$ the position of the i-th block the forces acting on it are:

- the first-neighbor elastic coupling: $k_1\nabla^2(\vec{h}_i)$;
- the driving plate elastic coupling: $k_0(\vec{h}_i - \vec{V}_0 t)$, where $\vec{V}_0$ is the driving plate velocity;
- the friction $\vec{\Phi}_i$.

The equation of the motion for the displacement of the block in one dimension then reads:

$$m\frac{d^2h_i(t)}{dt^2} = k_1(2h_i(t) - h_{i+1}(t) - h_{i-1}(t)) + k_0(h_i(t) - V_0 t) - \Phi_i(\dot{h}_i(t)), \qquad (2.1)$$

where $\Phi_i(\dot{h}_i(t))$, representing the friction, can depend on the block velocity in several ways. BK proposed a particular form for the friction term, including the effect of seismic radiation and Newton viscosity and assuming that, in the presence of viscosity, stresses are proportional to the strain rate.

The appreciation of the BK model by the physical community started after the statistical study performed by Carlson and Langer [50], who implemented a simpler velocity-weakening friction force:

$$\Phi_i(\dot{h}) = \begin{cases} [-\infty, \mu_S] & \text{for } \dot{h} \leq 0 \\ \frac{\mu_S - \delta}{1 - 2\alpha\dot{h}/(1-\delta)} & \text{for } \dot{h} > 0. \end{cases}$$

The static friction coefficient μ_S can be normalized to 1, via a change of variables, leading to only two parameters determining the friction law: δ, the instantaneous

drop of the friction when the slip starts (useful for numerical purposes), and α, the rate of weakening of the dynamical friction with the slip velocity.

Even in the case of the simplest friction law, defined by only two coefficients (static and kinetic) and applied to a single block, we already have an interesting stick-slip instability. In presence of many blocks, the finite slip of a single one may pull on neighbor blocks triggering an avalanche of numerous one-block slips, an event that can be identified with an earthquake. In the quasi-static limit of zero drive velocity $V_0 \to 0$, we can distinguish three separate time scales, one concerning the drive, the second (instantaneous if confronted with the first one) concerning the avalanche and the third (instantaneous confronted with the first and the second) concerning the single-block slip.

The occurrence of earthquakes in such a conceptually simple model triggered a large activity around the BK model: variations include two-dimensional blocks assemblies [51], models with long-range elastic interactions between blocks (which are an effective representation of the interactions via the bulk of the plate) [52], or driving via the system boundary (train model) [53]. The majority of studies on the BK model are focused on the magnitude distribution of events and its dependence on the friction parameters and, interestingly, with an appropriate choice of the parameters, such models are able to replicate the GR law.

The difficulty of simulating systems with a large number of blocks (due to the nature of the equations, i.e. coupled continuous ODEs), though, has pushed the statistical physics community to study simpler models in which general statistical results can be obtained, such as cellular automata representing sliding blocks.

2.2 Cellular Automata approach: Olami-Feder-Christensen Model

A cellular automaton model is a discrete model consisting of a regular grid of cells; every cell can be in one of a finite number of states. In 1989 Bak and Tang [55] have enlightened the similarity between stick-slip behavior in seismic occurrence and the evolution of a simple cellular automaton model. Subsequently Olami, Feder and Christensen (OFC) [2] explicitly show that the BK model, under the assumption

of a simple Coulomb friction and in the limit of vanishing driving velocity $V_0 \to 0$, can be mapped onto a continuous cellular automaton where the whole evolution is only controlled by the local force. We show this derivation in one dimension and we refer to the local force σ_i acting on the i-block. Equivalently, since we are working in lattice spacing units, σ_i can be viewed as the local stress.

Because of the sliding of the surrounding blocks and of the plate, following the Eq.2.1 the i-th block at time t experiences a force:

$$\sigma_i(t) = k_1(2h_i(t) - h_{i+1}(t) - h_{i-1}(t)) + k_0(h_i(t) - V_0 t). \tag{2.2}$$

The friction is supposed velocity-independent:

$$\Phi_i = \begin{cases} \sigma_i & \text{if } \sigma_i \leq \sigma_{th} \\ 0 & \text{otherwise.} \end{cases}$$

σ_{th} is the static friction threshold and the dynamic friction coefficient is set equal to zero. Furthermore we assume time scale separation.

Within these assumptions, the dynamics is the following: the force on the block i starts to grow, until it reaches its threshold value σ_{th}; at this point the force drops to zero, instantaneously in the drive timescale, and the new position of the block h_i' satisfies:

$$\sigma_i = k_1(2h_i' - h_{i+1} - h_{i-1}) + k_0(h_i' - V_0 t) = 0.$$

As a result, the displacement of the block will be:

$$\delta h_i = h_i' - h_i = -\frac{\sigma_i}{2k_1 + k_0}$$

and the change in stress on the neighbor blocks will be:

$$\delta\sigma = -k_1 \delta h_i = \sigma_i \frac{k_1}{2k_1 + k_0}.$$

This translates into simple rules for the stress σ_i acting on block i:

1) Assign a random initial value to every block $\sigma_i \in [0, \sigma_{th})$;

2) Increase all the σ_i uniformly at a constant rate $k_0 V_0$ until a block has $\sigma_i = \sigma_{th}$;

3) σ_i drops to zero, while all neighbors receive an additional pulse $\delta\sigma$;

4) If, because of the pulse, any neighbor's stress is increased over the threshold, repeat from step 3);

5) Otherwise, repeat from step 2).

The previous numerical implementation can be extended to any dimension d, providing that the stress increment $\delta\sigma$ now reads:

$$\delta\sigma = \frac{k_1}{n_n k_1 + k_0}\sigma_i,$$

where n_n is the coordination number of the d-dimensional lattice. The parameter

$$\alpha = \frac{k_1}{n_n k_1 + k_0}, \tag{2.3}$$

which can vary as $\alpha \in (0, 1/n_n]$, plays a central role in the model dynamics, being related to the amount of energy dissipated in each slip. After a given instability, indeed, only a fraction $n_n\alpha$ of the stress drop $\delta\sigma$ is redistributed inside the system, whereas $(1 - n_n\alpha)$ is given back to the external drive. The conservative case corresponds to $\alpha = 1/n_n$.

In order to clarify the relation between the size distribution in the OFC model and the GR law in seismic occurrence let us consider a 2d fault model. Since the block displacement $\overline{D}$ is roughly constant, an earthquake corresponds to a rigid slip of length D of a region of size A inside the fault. The seismic moment is defined as

$$M = k_1 a \sum_i \delta h_i,$$

where a is the lattice spacing, and, since $\overline{D}$ is constant in the OFC model, one has $M \propto A \propto S$, where S is the number of sliding blocks. The experimental GR

relation leading to $P(M) \propto M^{-(1+2/3b)}$ therefore corresponds to a size distribution $P(S) \propto s^{-\tau}$ where $\tau = 1 + 2/3b$.

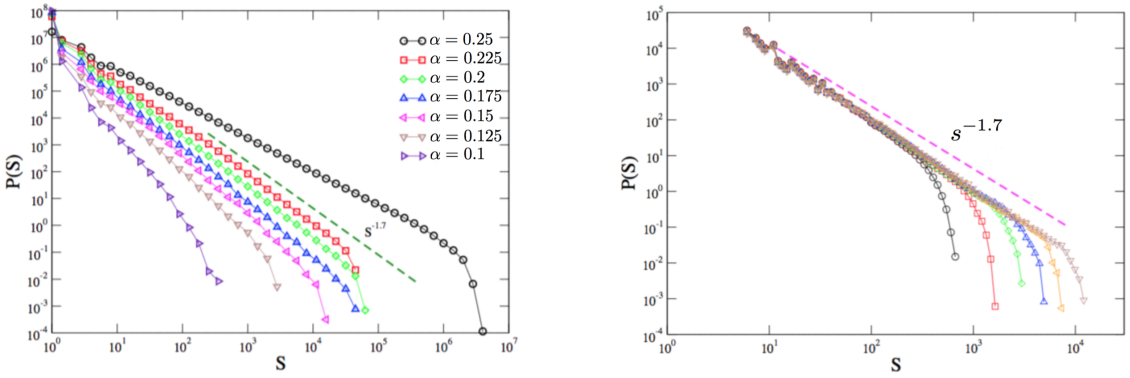

Figure 2.2: On the left side: the size distribution in the OFC model for a 2-dimensional lattice with $L = 350$ and different values of $\alpha \in [0.1, 0.25]$. The green dashed line is the expected experimental result $P(S) \sim S^{-1.7}$. On the right side: the size distribution in the OFC model for $\alpha = 0.2$ and different sizes $L = 32, 48, 64, 80, 96, 128$ from left to right. The magenta dashed line is the expected experimental result $P(S) \sim S^{-1.7}$ (adapted from [54]).

In Fig.2.2 we plot the size distribution $P(S)$ of the OFC model in $d = 2$. The power-law behavior of $P(S)$ indicates that the OFC model is able to reproduce the size distribution of seismic data at a qualitative level but not at a quantitative one, in the conservative case $\alpha = 1/4$ since the numerical value of $\tau \simeq 1.1$ is much smaller than the experimental one, $\tau \simeq 1 + 2/3$. Interestingly, though, as you may see in Fig.2.2 (left side), OFC model studies the dependence of the exponent τ on the dissipation parameter α, finding a α-range in which τ has a good agreement with experimental data. About the finite size effects, it has to be observed that the initial power law decay is not involved, being the same for different sizes, as you can easily check in Fig.2.2 (right side); what actually does change with size is the cut-off of the distribution for large sizes, which becomes larger as the size grows; this suggests that, in the limit $L \to \infty$, the power law decay stands at all sizes.

Observe that in this model we considered open boundary conditions; it was proven [11] that the power law behavior of this model stands also with free bound-

ary conditions, but not with periodic boundary conditions.

As a final remark, notice that the OFC prediction $M \propto A$ is in disagreement with experimental data $M \propto A^{3/2}$ [24]. This discrepancy comes from the fact that, while in the OFC the average slip $\overline{D}$ is intrinsically constant, in the real systems it varies with the size of the event.

2.3 Self Organized Criticality

Introduced by Per Bak and his colleagues [4], Self Organized Criticality (SOC) has played a significant role in the development of complexity science. Complexity arises in the sense that no single characteristic event size exists, i.e. no scale present to guide the system's evolution.

In their seminal work Bak et al. provided one of the first principles unifying the origins of the power law behavior observed in many natural systems. The core hypothesis was that systems consisting of many interacting components will, under certain conditions, spontaneously organize into a state with properties akin to the ones observed in a equilibrium thermodynamic system near a second-order phase transition. As this complex behavior arises spontaneously without the need for external tuning this phenomena was named Self-Organized Criticality.

The highly appealing feature of the SOC theory is its relation to the well established field of the phase transitions and the notion of universality. The universality hypothesis groups critical phenomena, as observed for many different physical phase transitions, into a small number of universality classes. Systems belonging to the same universality class share the values of critical exponents and follow equivalent scaling functions. This universal behavior near a critical point is caused by a diverging correlation length. The correlation length becomes much larger than the range of the microscopic interactions, thus the collective behavior of the system and its components becomes independent of its microscopic details. This also implies that even the simplest model captures all the aspects of critical behavior of the corresponding universality class.

Physical systems which are believed to exhibit SOC behavior are usually characterized by a constant flux of matter and energy from and to the environment. Thus, they are intrinsically non-equilibrium systems. The concept of universality

is still applicable to non-equilibrium phase transitions. However, an universal classification scheme is still missing for non-equilibrium phase transitions and the full spectrum of universality classes is unknown. The properties of non-equilibrium transitions depend not only on the interactions but also on the dynamics. In contrast, detailed balance, a necessary precondition for an equilibrium state, constrains the dynamics in equilibrium phase transitions.

Phenomena of strikingly different backgrounds were claimed to exhibit SOC behavior: sandpiles, earthquakes, forest fires, rivers, mountains, cities, literary texts, electric breakdown, motion of magnetic flux lines in superconductors, water droplets on surfaces, dynamics of magnetic domains, growing surfaces, human brains, etc (for further references [54]). Neglecting the specific details of each model, here we summarize their common features:

- Lattice models: usually all these systems are represented on a discrete lattice;

- Threshold mechanism: local instability happens as soon as a threshold value of some variable is reached; as a consequence, by means of local interactions, all the system is globally rearranged (avalanche);

- Time scales separation: the external drive is much slower than the typical time scale of the local instability and of the avalanche propagation, which in these models is usually considered instantaneous;

- Dissipation: a form of dissipation is always present, often by means of open-boundary conditions;

- Power laws: the scale-free avalanche size distribution is the distinct feature of SOC systems.

In the following section we will explain in detail the sandpile model, the original model studied by Per Bak et al, in order to enlighten the main mechanisms leading to SOC behavior.

2.3.1 Sandpile model

Sandpile model (or Bak-Tang-Wiesenfeld model), as we mentioned, was the first of a series of very simple models which evolve towards a critical state without external tuning [4]. Quite interestingly, in its first version (Bak et al, 1987) it was derived for the dynamics of an array of coupled oscillators, in order to find the origin of pink noise. We stressed this aspect because, in this thesis work, we are going to focus on the role of synchronization in the avalanche dynamics, and it is useful from this point of view keeping in mind that these simple stick-slip models can describe systems of global and local coupled oscillators.

The BTW model is defined on a quadratic 2-dimensional lattice; the state of each site (i, j) is characterized by an integer non-negative variable $u_{i,j}$. In analogy with a sandpile, we can think to the integer number $u_{i,j}$ as the number of grains stacked on top of each other at the site (i, j). In every discrete time step, a site is randomly chosen and the correspondent variable is incremented by one: $u_{i,j} \to u_{i,j} + 1$, which corresponds to adding a grain to the grain pile in the site; if the condition $u_{i,j} < 4$ is verified, another time step is made, otherwise the stack of grains in (i, j) is no longer stable and the four grains are uniformly redistributed among the four nearest neighbors; this reads as all four neighbors of the unstable site incremented of one, while the unstable site decremented of four; the neighbors, as a consequence, can be unstable as well. Once the instability propagation (avalanche) is over, the system goes on with the next time step. This translates into a simple implementation for $u_{i,j}$ evolution:

1) Assign a random initial value to every site $u_{i,j} \in [0, 1, 2, 3]$;

2) Choose randomly one site (i, j) and increment its u-value of one: $u_{ij} \to u_{i,j} + 1$;

3) If $u_{i,j} < 4$, repeat from 2);

4) Otherwise, $u_{i,j} \to u_{i,j} - 4$, while all its neighbors are incremented by one:

$u_{i,j\pm1} \to u_{i,j\pm1} + 1$ and $u_{i\pm1,j} \to u_{i\pm1,j} + 1$;

5) If this instability has generated new instabilities, repeat from 4);

6) Otherwise, repeat from 2).

In Fig.2.3 we reported an example of an avalanche in such a system. Observe that the toppling rule 4) is conservative, in the sense that the total number of grains remains constant during an avalanche. This corresponds to the OFC model without dissipation ($\alpha = 1/n_n$). As soon we implement some dissipation the situation changes, as it happened with the implementation of the model by Feder and Feder [56], where the toppling rule for the unstable site was: $u_{i,j} \to 0$, instead of $u_{i,j} \to u_{i,j} - 4$. This version of the model differs from the original one only if $u_{i,j} > 4$ temporarily. The third stage in Fig.2.3 shows that this case may occur during an avalanche.

Actually, while the distribution of the grains on the neighbors is indeed conservative, the fact that at each time step we introduce a new grain in the system could lead to an infinite avalanche situation; in order to prevent that, it is important to introduce in the model open boundary conditions. In this situation the avalanche size, which corresponds to the number of sites involved in an avalanche, follows a power law distribution, with an exponent $\tau \simeq 1.1$, as we mentioned before.

As a final remark, notice that the BKW model is an abelian model, which means that the final result of the avalanche does not depend on the order of the topplings performed.

2.3.2 The generalized BTW model

The generalized BTW is a model in between the original BTW model and the OFC model [6]. On one hand we have continuous site variables and an uniform drive as in the OFC model, on the other the dissipation is implemented in an updating rule very similar to the original one in the BTW model, where the variable site is decreased of a fixed amount as the site becomes unstable.

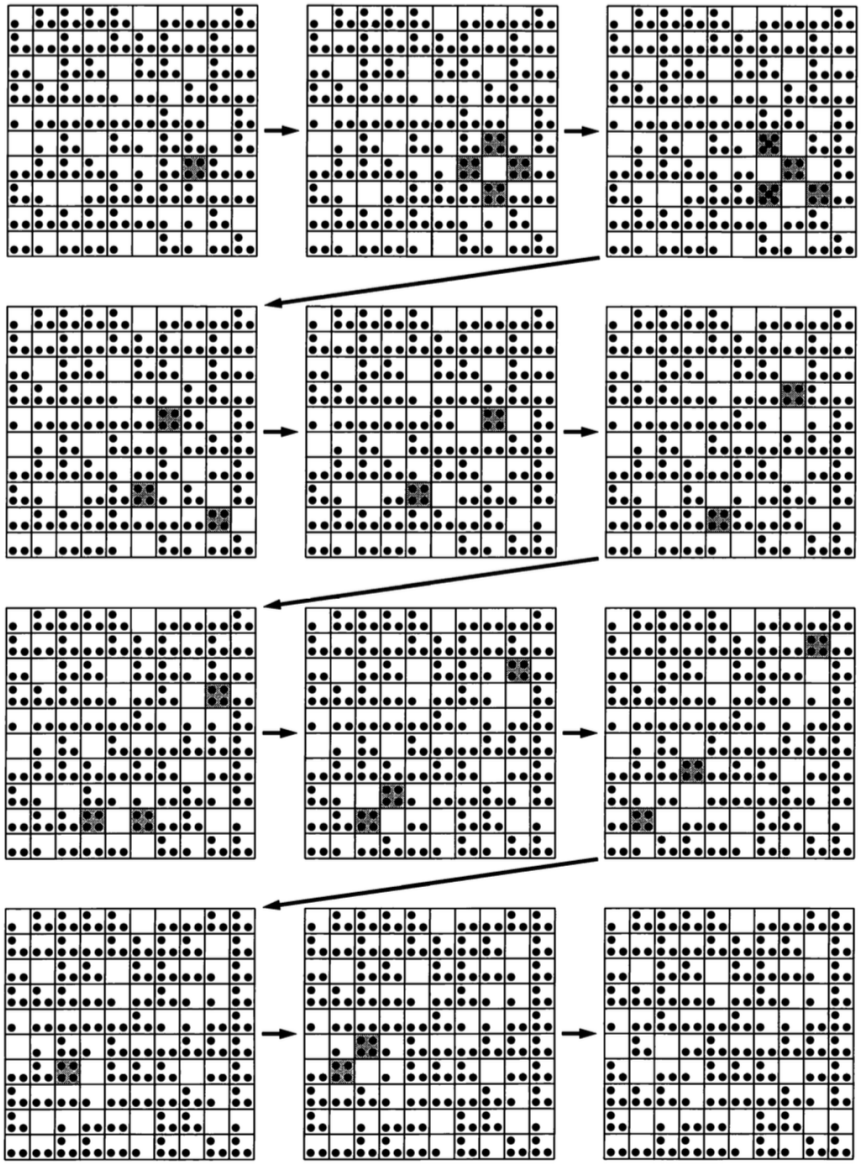

Figure 2.3: Evolution of an avalanche in the sandpile model; here every square represents a site, while dots represents the grains stacked in the site; activated sites are marked in grey (adapted from [49]).

Recovering the terminology we used in the explanation of the OFC model, the dynamics is the following:

1) Assign a random initial value to every block $\sigma_i \in [0, \sigma_{th})$;

2) Increase all the σ_i uniformly at a constant rate $k_0 V_0$ until a block has $\sigma_i = \sigma_{th}$;

3) σ_i drops to $(\sigma_i - \sigma_{th})$, while all the n_n neighbors receive an additional pulse:

$$\delta\sigma = \alpha\sigma_{th} = \frac{k_1}{n_n k_1 + k_0}\sigma_{th};$$

4) If, because of the pulse, any neighbor's stress is increased over the threshold, repeat from step 3);

5) Otherwise, repeat from step 2).

The constant α determines the conservation level. When $\alpha < 1/n_n$, where n_n is the coordination number of the lattice, an amount equal to $(1 - \alpha n_n)\sigma_{th}$ is lost as a consequence of the update.

Numerical simulations performed on a 2-dim lattice show that, for $\alpha = 1/n_n$ (conservative limit), the avalanche size distribution is a power law with an exponent $\tau \simeq 1.05$, and a cut-off that diverges with the size of the system.

As long as we introduce some dissipation, the distribution starts to present smaller cut-off as α is decreased, and it is well fitted by the function:

$$P(s) \propto s^{-1} \exp\Big(- \frac{s}{s_{max}} \Big)^{1.3}$$

The cut-off s_{max} dependence from the dissipation α follows:

$$s_{max} \sim \Big(\frac{1}{n_n} - \alpha \Big)^{-1}$$

Moreover, if we look at the avalanches in time, we notice a periodic behavior that tends to disappear in the limit $\alpha \to 1/n_n$. In Fig.2.4 we report numerical results for several value of the dissipation α.

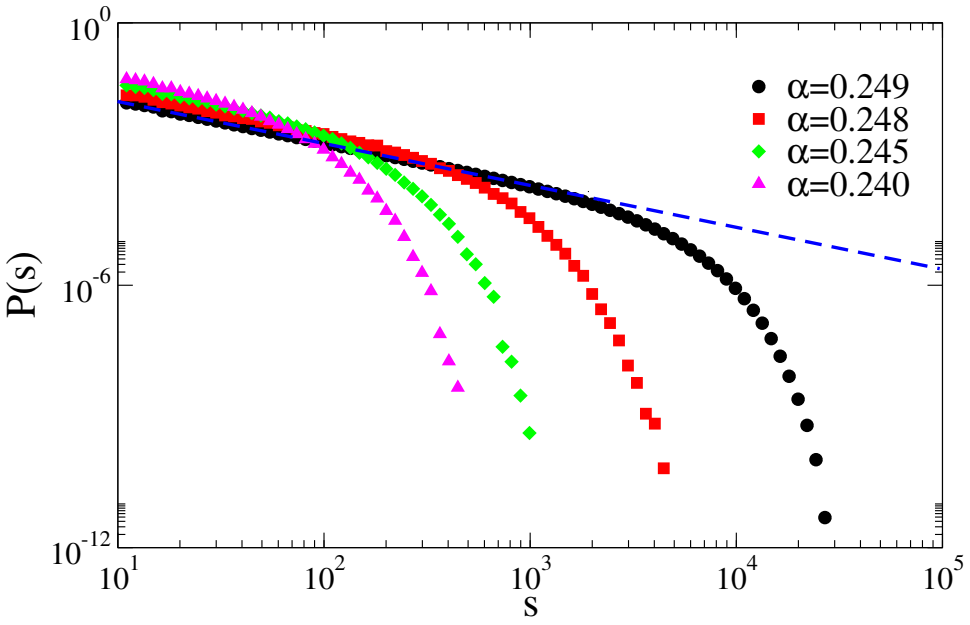

Figure 2.4: Numerical evaluation of the avalanche size distribution for a 2-dimensional lattice with $L_x = L_y = 200$, for decreasing values of the parameter α ($\alpha = 0.25$ is the conservative limit). The critical behavior is indicated by the blue dashed line $s^{-\tau}$, where $\tau = 1$.

Chapter 3

The role of randomness in the SOC behavior of the models

In this Chapter we introduce the problem of the elastic interfaces driven in a random media. Interestingly, this model can be mapped into a cellular automata one, the OFC* model, which implements annealed disorder in the OFC model previously discussed. We report the results of 2-dim simulations of this model and of a slightly different version, where more disorder is added.

3.1 Elastic interfaces driven in a random medium: the depinning transition

The problem of driven elastic interfaces is a phenomenon deeply investigated in condensed matter physics since it is encountered in a large variety of situations starting from the simple evolution of interfaces between magnetic domains up to the dynamics of dislocation assemblies such as vortices in superconductors or charge density wave materials [57]. The common features of all these systems are the short-range nature of the interactions and the dominant role of viscous forces over inertial terms. This connection between apparently distant problems allows to implement methods and procedures developed within one context to get further insights in the other problem. The relation between the SOC and the interfaces problem has emerged after the seminal paper by Hwa and Kardar (HK) [58]. HK

describe the height profile of a sandpile by means of a Langevin equation including an additive thermal-like noise. This description allows to obtain some insights in the mechanisms responsible for criticality but does not apply immediately to SOC like models presenting the features listed in the previous chapter; in particular, the threshold mechanism is not considered in the Langevin equation approach. In the following we will present the model in the more general way and in the next section we will see how it is related with SOC systems.

Let us consider the interface as a line of defects aligned, for instance, along the x direction and indicate with $h(x,t)$ the displacement at time t in the perpendicular direction z. Assuming nearest-neighbor elastic interactions and neglecting inertial effects the velocity along the perpendicular direction is given by:

$$\eta \frac{\partial h(x,t)}{\partial t} = \nabla^2 h(x,t) + F_D, \tag{3.1}$$

where η is the viscosity coefficient, the term $\nabla^2 h(x,t)$ comes from a gradient expansion of the short-range Hamiltonian (the elastic approximation) and F_D is a driving force. In the case of interfaces between magnetic domains, for instance, the driving force is an external magnetic field and the elastic term describes the ferromagnetic interaction. Very interesting patterns are observed in presence of local impurities, such as a random field acting on the system that can be modeled as an extra random force Φ in Eq.3.1:

$$\eta \frac{\partial h(x,t)}{\partial t} = \nabla^2 h(x,t) + F_D + \Phi(h(x,t)). \tag{3.2}$$

By noticing that for a discretized system $\nabla^2 h(x,t) \propto 2h_i(t) - h_{i-1}(t) - h_{i+1}(t)$ it is evident the analogy between the above equation for the interface displacement h, usually known as the quenched Edward-Wilkinson equation [59], and Eq.2.1 controlling the evolution of the block position in the BK model. Indeed, adding a viscous term in Eq.2.1 and assuming that inertial effects can be neglected, as in the OFC model, one obtains an equation which is formally identical to Eq.3.2, where F_D and Φ are the drive and the friction force, respectively. The only qualitative difference is that in the BK model $h(x,t)$ corresponds to displacements in the plane direction whereas, for an interface, displacements are perpendicular to the

defect line. This formal analogy reflects in a similar behavior observed, in particular, when the driving force F_D approaches a critical value. The interface motion just below the threshold, consists of abrupt jumps, as large segments of the interface depin from strong pinning centers (impurities), followed by periods without significant displacements. These jumps, conceptually equivalent to earthquakes in the BK model, provide an explanation for the so-called Barkhausen noise [60] measured in ferromagnetic materials, i.e. the experimental observation of abrupt jumps in the magnetization due to flipping of magnetic domains via avalanches, whose sizes follow a power-law distribution. It is possible to simplify the analysis of the dynamics arising from Eq.3.2 if we use for the disorder landscape the Narrow Well Approximation [61] [62]: the idea is that pinning centers are very localized in space. If a block reaches one of these positions it falls inside the well and it is completely locked unless the total force reaches a threshold $F_{th}(h(x,t))$ which allows to overcome the depth of the well. The block, then, moves over a distance δh until it finds another well. The other hypothesis is that the force-drop, corresponding to this displacement, is much smaller than the well depth. Under this assumption the block abruptly jumps from one well to the subsequent one.

3.1.1 The depinning transition with constant driving force

Eq.3.2 is usually studied assuming a constant F_D. We will see what happens to the dynamics in different driving-force F_D regimes.

Pinned phase If we start from a very small force, the interface will easily be pinned. As we increase the force, at some point the interface can escape from the impurity. This may cause the neighboring impurities to also detach right after the next one, and then their own neighbors, and so on, almost instantaneously (on a time scale η^{-1}). This chain reaction or avalanche stops when the interface is finally pinned down and the local velocity is zero everywhere. If we again increase the force by an infinitesimal amount δF, a new avalanche may be triggered. Keeping the perturbation δF constant, for larger forces F_D, the interface will need to find stronger impurities in order to stop, something that will become more rare: the avalanches will get bigger with increasing F_D (and constant δF).

Depinned phase Above a certain force, the occurrence of impurities strong enough to pin the entire line will switch from rare to non-existent, so that the center of mass will never rest: we say that the interface is depinned, and we have:

$$\begin{aligned} v(t) &> 0 \quad \forall t, \qquad \text{where} \\ v(t) &= \langle \partial_t h \rangle = \frac{1}{L^d} \int \partial_t h(x,t) d^d x \end{aligned}$$

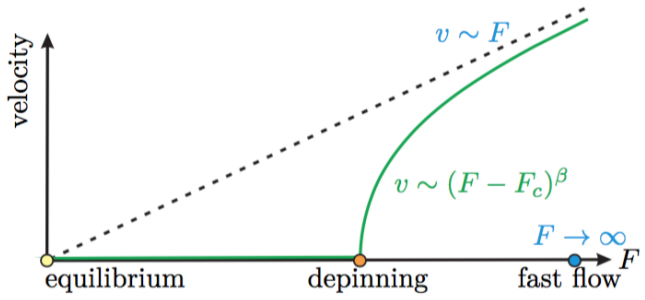

Figure 3.1: Adapted from [8]: Depinning transition at zero temperature.

So for small F_D the system is in the *pinned state* whereas for large F_D is in the *slipping state*. There exists a specific value $F_D = F_c$ where a transition between the two dynamical states is found. This transition exhibits very striking similarities with standard phase transitions at the critical point. Indeed, one can consider the interface velocity v as the order parameter which close to F_c exhibits the following behavior:

$$\begin{cases} v = 0 & \text{if } F_D < F_c \\ v \propto (F_D - F_c)^\beta & \text{if } F_D \gtrsim F_c \end{cases}$$

In Fig.3.1 we report a qualitative representation of the transition.

Close to $F_D \simeq F_c$ the typical patterns observed at the critical point, such as the diverging susceptibility, as well as the power law in the size distribution, can be all related to the divergence of the correlation length ξ, i.e. the typical distance l over which $h(x)$ and $h(x+l)$ are correlated. The above observations imply that

even if depinning, under a constant external force, is a transition between non-equilibrium dynamical states, it can be interpreted in the general framework of classical critical phenomena.

Up to now we have not yet discussed in detail the statistical properties of the avalanches which are also expected to display critical behavior at the transition. Above the threshold (depinned regime), the dynamics consists essentially in numerous almost independent avalanches. However when a point is almost stopped (just before the end of an avalanche) it may keep on moving by participating in a new one: because the motion truly consists in a single very large, never-ending avalanche, these are not really independent. This makes it difficult to properly define finite avalanche events, above the threshold. Below the threshold (pinned regime, $F < F_c$), an infinitesimal increase δF of the force may trigger avalanches. By taking δF small enough, as we mentioned before, one may hope to ensure that exactly zero or one avalanche will be triggered. In this way, one can a priori trigger a large number of avalanches at fixed F , given that $\delta F \ll |F_c - F|$. However numerically it may prove difficult to keep F constant while increasing it by δF several times. For these reasons in the next section we will introduce another way to drive the system, which is more relevant for frictional or seismical applications and allows for unlimited avalanche statistics while staying below the critical force F_c.

3.1.2 The depinning transition with elastic driving force

Instead of driving the system with a constant force F_D equal in all points of the interface and independent of its progression, we can pull it elastically via springs (one per site) attached to a common surface (set in the plane $z = w$) with an externally imposed velocity V_0 (i.e. $w = V_0 t$), as we did in the BK model. The equation now reads:

$$\eta \frac{\partial h(x,t)}{\partial t} = k_1 \nabla^2 h(x,t) + k_0 (V_0 t - h(x,t)) + \Phi(h(x,t)). \tag{3.3}$$

The dynamics that arises from such a system is very similar to the previous case but, since the driving force is no longer constant, it cannot be the control parameter

any more. What we can control is the driving velocity V_0 (and the stiffness k_0). In order to get a stationary driving term $k_0(V_0t-h)$, to a macroscopic increase of the drive $\Delta F = k_0 V_0 \Delta t$ must correspond an interface displacement $\Delta h \sim V_0 t$. In this case the averaged (in space and in time) interface velocity will be: $\langle v \rangle = V_0$. For an infinite system there will always be a point of the interface moving (i.e. some avalanche occurring) and the time average on v does not need to be taken over a long interval Δt, i.e. we have an instantaneous space-averaged velocity $v(t) = V_0$.

The stress or force $\sigma(x,t) = k_0(w-h)$ is now a response function, and we find that the time and space averaged quantity $\sigma(V_0)$ follows the same behavior of $F(v)$ in the constant driving force case. Indeed, the situation $V_0 = 0^+$ corresponds to the limit $v \sim |F_c - F|^\beta \sim 0^+$. Thus, the elastic driving method (in its stationary regime) does not allow to explore the whole region $F < F_c$ of the phase diagram. Instead, it automatically drives us to the critical point, which is much more interesting. The situation, varying V_0, is the following:

- At $V_0 = 0$, after a possible short transient, nothing happens and we have $\sigma - k_0 h < F_c$ everywhere: we are below criticality.

- At $V_0 = 0^+$ i.e. in the quasi-static regime, the system evolves via discrete and well-defined avalanches. At the end of each avalanche, the system is stable and $\sigma - k_0 h < F_c$ everywhere, but this never lasts: the system oscillates around the critical point.

- At any finite velocity $V_0 > 0$, the infinite system is always in motion and we are above the critical point.

The critical velocity is $V_0^c = 0^+$.

The restoring force $-k_0 h(x,t)$ decreases the driving force when an avalanche unfolds, allowing to automatically set ourselves at the depinning transition critical point; we do not need to tune any parameter to go there, we may recognize this as an example of Self-Organized Criticality (SOC).

Since we are automatically driven towards the critical point, we expect that all quantities of interest, in particular the correlation length ξ will diverge to

infinity. However, during an avalanche the term $-k_0 h$ actually takes us a bit below criticality. We now need to characterize quantitatively how far we typically are from criticality, depending on k_0 (keeping $V_0 = 0^+$).

The key observation is that the correlation length ξ corresponds to the typical length scale where the contribution of the energy input from outside:

$$E_{drive} \propto K_0(V_0 t - h)^2$$

is balanced by the elastic energy

$$E_{elastic} \propto (\nabla h(x,t))^2.$$

More precisely

$$E_{drive}(\xi) = \frac{1}{2}\int_{\xi^d} d^d x k_0 (V_0 t - h(x,t))^2 \sim E_{elastic}(\xi) = \frac{1}{2}\int_{\xi^d} d^d x k_1 (\nabla h(x,t))^2.$$

From a simple dimensional analysis $E_{drive}(\xi) \sim k_0 \xi^d h^2$ whereas $E_{elastic}(\xi) \sim k_1 \xi^{d-2} h^2$ leading to:

$$\xi \sim \left(\frac{k_0}{k_1}\right)^{-\frac{1}{2}} \tag{3.4}$$

This result, rigorously derived from field theory [63], shows that a critical state $\xi \to \infty$ can be only achieved if $k_0/k_1 \to 0$.

The presence of a finite (k_0/k_1), conversely, introduces deviations from criticality that appear as an upper cut-off S_m in the size distribution:

$$P(S) = S^{-\tau} f(S/S_m) \tag{3.5}$$

where $f(s)$ is a scaling function which decays very fast when the argument is greater than 1. S_m, indeed, is directly related to ξ:

$$S_m \sim \xi^{d_f}, \tag{3.6}$$

where d_f is the fractal dimension of the volume spanned by a two-dimensional interface.

It is possible [66] to relate τ to d_f, making the following considerations. Since each avalanche S is the response Δh to an infinitesimal increase $\delta F = \Delta F/N$, the average response to an increase of the force ΔF will be the sum of the avalanche sizes for the infinitesimal increases. Now using an argument similar to the one we used to obtain $v = V_0$, we obtain:

$$\langle S \rangle \sim \frac{\Delta h}{\Delta F} \sim \frac{1}{k_0}.$$

On the other hand, we can calculate $\langle S \rangle$ by means of its probability distribution:

$$\langle S \rangle = \int SP(S)dS \sim S_m^{2-\tau} = (\xi^{d_f})^{2-\tau}. \tag{3.7}$$

Remembering the scaling of ξ with k_0, by identification we obtain:

$$\tau = 2 - \frac{d}{d_f}.$$

3.2 Mapping the elastic interfaces model on a cellular automaton one: the OFC* model

A cellular automaton version for the interface evolution can be obtained by mean of a discretized description of the elastic interface as blocks interconnected by springs. As we mentioned at the beginning of the chapter, a crucial point to map the elastic interface in a random medium onto a discrete model is the narrow well approximation [61] for the friction landscape, which now we discuss in detail.

In Fig.3.2 we report a schematic representation of this kind of system in one dimension. Physically, the disorder energy landscape is seen as a collection of narrow wells representing impurities. Along the h direction, the narrow wells are separated by random intervals z drawn by a random distribution $g(z)$. A natural choice for $g(z)$ is the exponential law, which corresponds to the case where impurities are uncorrelated in space and therefore obey a Poisson distribution.

The value of the disorder force in a well depends on its shape, essentially defined by the width along the h direction and the depth. We will assume that

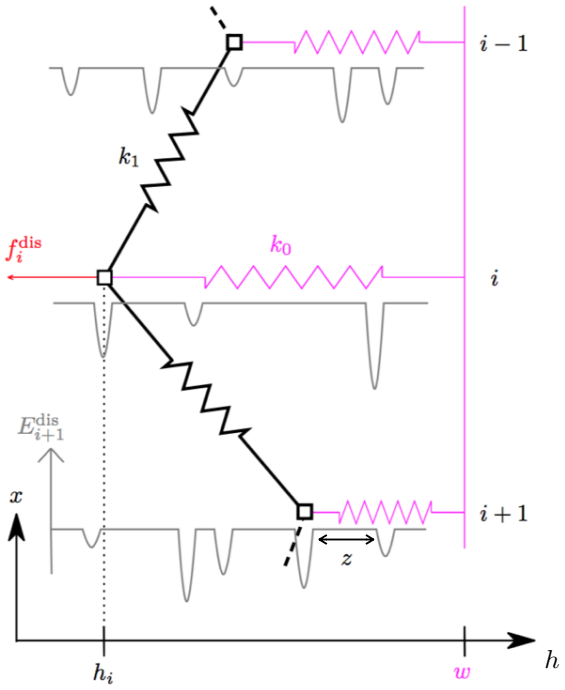

Figure 3.2: Mechanical sketch of the one-dimensional elastic interfaces model with elastic drive (adapted from [61]): the interface (black bold line) is made of blocks (empty squares), in discrete positions along the x-axes, connected to each other by springs (k_1). The blocks are connected to the driving surface w by other springs (k_0); they also experience the disorder force representing the friction: the disorder force f_i^{dis}, that acts on the i-th block, comes from a disordered energy potential E_i^{dis}, which is simplified as a series of narrow wells separated by random spacings.

the width is much smaller than the depth; furthermore, we will consider the wells narrow, i.e. their widths are negligible compared to z, so that the displacement of a point trapped in a well is negligible compared to the jumps between wells. As a consequence any time a site escapes from a well, it will directly jump to the next one, never staying in between two wells; to exit from a well, a block will need to be pulled by a force larger than some threshold σ_i^{th} related to the well's depth. A given random distribution of depths correspond to a random distribution for the threshold forces f_i^{th}.

If now we consider the interface as a collection of blocks in discrete positions along the x axes, under these assumptions, the continuous dynamics of the blocks becomes fully discrete. As long as each site fulfills the stability condition:

$$k_0(Vt - h_i(t)) + k_1 \nabla_i^2 h(t) < f_i^{th}, \qquad \forall i \in L^d, \tag{3.8}$$

(where $\nabla_i h$ is the discrete laplacian of the block displacement h_i), the interface does not move at all. When the increase of the force is enough to violate Eq.3.8 in one point i, the interface locally jumps forward to the next well, i.e. h_i increases by z (drawn from $g(z)$), and a new threshold force f_i^{th} is drawn at random. The new value of h_i changes the laplacian term in Eq.3.8 and it can trigger further instabilities in the connected sites. This process is iterated until Eq.3.8 is valide for all the sites in the system.

This leads to a numerical protocol very similar to the OFC one, outlined in the previous chapter. The interface evolution can be then described by the same set of rules used for the OFC dynamics. The only differences are:

- After an instability, the force drop $\delta\sigma_i$ is equal to $(k_0 + n_n k_1)\delta h_i$, where n_n is the number of first neighbors of the site i and $\delta h_i = z$; this force drop is independent of the value of σ_i, whereas in the OFC model $\delta\sigma_i$ is proportional to σ_i. The above stress drop produces a force increment $k_1\delta h_i$ in the surrounding blocks. Therefore, as in the OFC model, the quantity α defined in Eq.2.3, is still related to the amount of energy dissipation in each local displacement;

- The force thresholds are random, and they change after every instability.

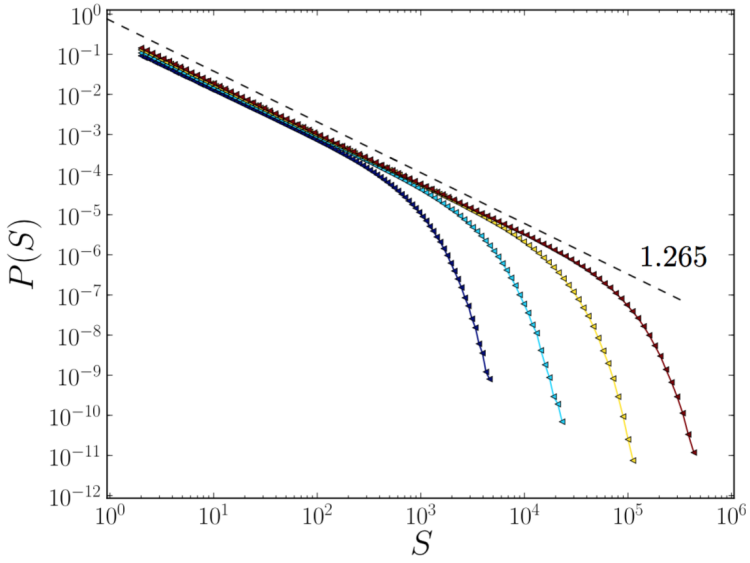

Figure 3.3: Probability distribution $P(S)$ of avalanches in the OFC* model for different values of the ratio $k_0/k_1 = 0.03, 0.01, 0.003, 0.001$ from left to right. The dashed line indicates the best fit power-law decay $P(S) \sim S^{-1.265}$. (From [61]).

Since the only differences with the OFC model is the randomness in the friction thresholds and force drop, this model is sometimes defined as the OFC* model [65]. In Fig.3.3 we present results of numerical simulation of a two-dimensional ($n_n = 4$) OFC* for the distribution of the avalanche size S, corresponding to the area explored by the interface during a jump. The distribution is consistent with the scaling law we discussed in the previous section, with $\tau \simeq 1.265$.

Numerical results, supported by analytical arguments, indicate that in the OFC* model a "critical" state can be obtained only in the limit $k_0/k_1 \to 0$ according to Eq.3.4. Under the assumption that the same arguments also hold for the OFC model one would expect that a critical state can be only observed in the limit $\alpha \to 1/n_n$ (Eq.2.3) corresponding to absence of dissipation in the OFC model. Nevertheless, we wish to observe that the size distribution behaves in a very different way in the OFC and in the OFC* model as the parameter α is changed. Indeed, as shown in Fig.2.2 and Fig.3.3, in the OFC* model α affects only the upper cut-off S_m whereas the exponent τ is left unchanged. Conversely, in the OFC model, the exponent τ appears to depend on α whereas S_m is mostly

influenced by the system size.

3.2.1 The modified OFC* model

We performed numerical simulations for a modified version of the OFC* protocol, where the thresholds have a fixed value:

$$\sigma_i^{th} =, 1 \quad \forall i$$

while the jump z is drawn from a random distribution every time a site topples. The aim is to understand if the introduction of quenched disorder in just one parameter of the dynamics is a sufficient condition for the stability of the critical behavior with dissipation. Indeed, as you may check in Fig.3.4, where we report a comparison of the two models in the subcritical region, the avalanche size distribution is pretty much the same, with the same exponent of the power law behavior. What does slightly change between the two models is the cut-off of the distribution, but the critical behavior is the same. We deduce that the stability of the exponent is independent on how much disorder we introduce in the model.

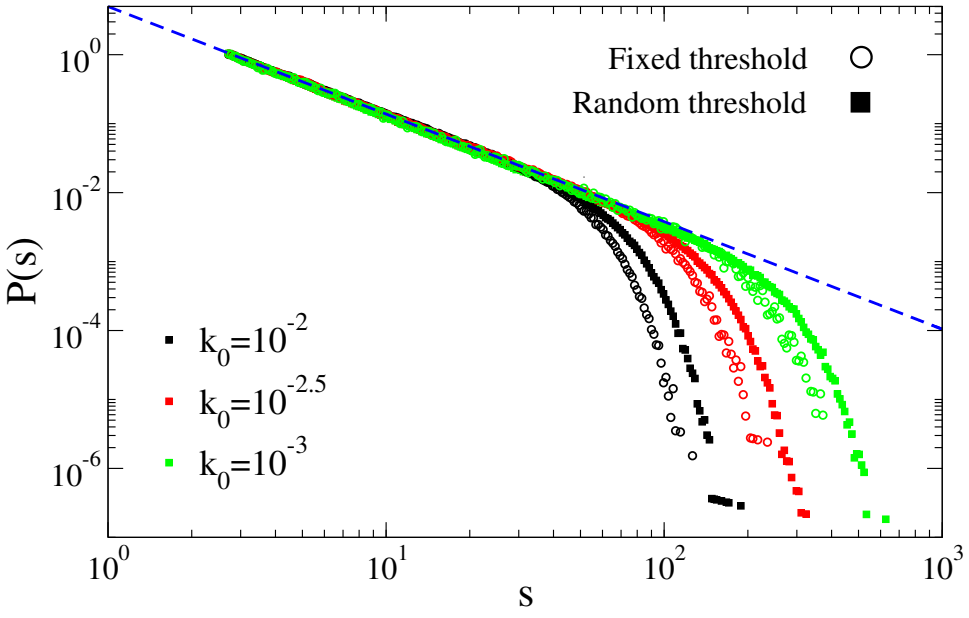

Figure 3.4: A comparison of two versions of the OFC* model, with fixed or random thresholds, for different values of k_0 ($k_0 \to 0^+$ from left to right). The system has size $L = 512$. The dashed blue line $s^{-1.3}$ is reported as a guide to the eye for the power law behavior.

Chapter 4

The role of visco-elasticity in the SOC behavior of the models

In this Chapter we discuss the introduction of viscosity in the models previously presented.

4.1 Viscous coupling

The idea that viscosity could be a possible key to model aftershock occurrence in spring-block models was first introduced by Burridge and Knopoff. In the early 1990s Nakanishi [73] presents a one dimensional spring-block model coupled viscoelastically to the driver plate, in order to represent the viscous coupling with the asthenosphere. The system is mechanically homogeneous and disorder is implemented only through initial stress conditions. This model reproduces the GR law only for a specific value of the stiffness but, most importantly, aftershocks are generated with a rate decaying according to the Omori law with an exponent p dependent on model parameters. A more complete model has been proposed by Hainzl et al. [74], where a one-dimensional chain of elastically coupled blocks is bound by springs to an intermediate set of blocks. This intermediate set, in turn, is coupled via dashpots to the drive, modeling the viscous asthenosphere and modifying equilibrium position after the slip of each block on the fault. For particular parameter values, the model is able to provide not only a size distribution con-

sistent with the GR law, but also a realistic number of aftershocks following the Omori law. Unfortunately, the behavior clearly depends on the initial random distribution of stress on the blocks.

A further study by Pellettier [75] has shown that the combination of viscous coupling and heterogeneous friction is able to produce, in spring-block models, temporal seismic clustering before and after large events: aftershocks are observed to decay according to the Omori law with an exponent $p \simeq 1$ that appears to be quite independent of seismic coupling. Moreover, the model presents seismic activity consistent with the GR law for small events whereas the large magnitude behavior changes from characteristic earthquake behavior, for large seismic couplings, to a GR distribution with a magnitude cutoff, for low seismic couplings. An inverse Omori law is also found for foreshocks. In particular, the ratio of foreshocks to aftershocks decreases with decreasing seismic couplings, from a value near one for a system exhibiting characteristic earthquake behavior to a value much smaller than one in absence of characteristic events. Thus, the model suggests that the relative number of foreshocks to aftershocks is related to whether the fault displays or not characteristic earthquake behavior.

4.2 Viscous coupling in the OFC model: the OFCR model

In this section we study the influence fo viscosity on the dynamics of the cellular automata version of spring-block models. The so-called OFCR model, proposed by Jagla [7], introduces in the OFC* model a relaxation mechanism that acts on a time scale τ_R in between the instantaneous one of the avalanches (τ_0) and the slow one of the drive (τ_D):

$$\tau_0 \ll \tau_R \ll \tau_D.$$

This mechanism leads to a smoothing of the stress field of the OFC* model over time, which is reasonable if we consider relaxation as a way to model the effect of the microscopical processes related to viscosity. Remembering, as we mentioned in the dimensional analysis in sec. 2.2, that we are working in lattice spacing units,

the evolution of the stress for the inter-avalanche time in the OFCR model reads:

$$\frac{d\sigma_i}{dt} = k_0 V_0 + R\nabla^2\sigma_i; \tag{4.1}$$

the first term is the usual drive whereas the second one corresponds to the relaxation. These two terms introduce two different timescales: $\tau_0 \sim V_0^{-1}$ and $\tau_R \sim R^{-1}$. Thus, the relevant parameter of the dynamics of the system will be the ratio R/V_0, that measures the competing effect between relaxation and the global driving.

All the σ_i evolve according to Eq.4.1 until the first block becomes unstable. This can happen because of the drive or because of the relaxation. When a site topples the stress is redistributed as in the OFC* model.

This model and a few variants of the relaxation mechanism in Eq.4.1 were studied in great detail in [7] [65], via numerical simulations. Interestingly, several features observed are in good agreement with the earthquake phenomenology.

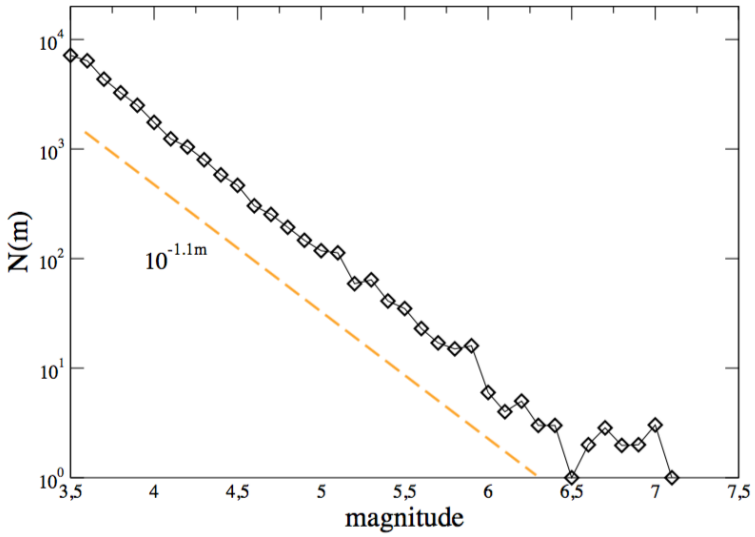

Figure 4.1: The magnitude distribution of the OFCR model for a system of size $L = 1000$. The dashed orange line is the GR law $N(m) \simeq 10^{-bm}$ (From [54]).

For R/V_0 sufficiently large, the avalanche size distribution displays a stable power law behavior with an exponent $\tau \simeq 1.7$, the same value of the empirical GR

law case. In Fig.4.1 we reported an example. The exponent is independent from the dissipation parameter α, that is related only to the cut-off of the distribution.

Another interesting consequence of the relaxation mechanism is the presence of aftershocks as side-effects of main shocks, as they continue to occur after a main shock, even when driving is stopped. In Fig.4.2 we report an example in one dimension in order to understand how this happens.

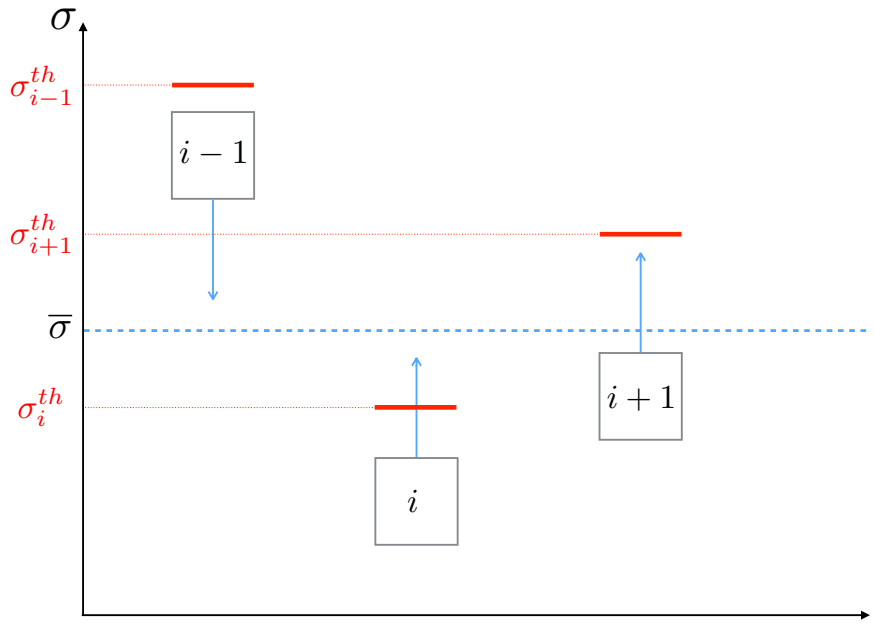

Figure 4.2: A picture of the stress of three sites, the site i and its neighbors $i-1$ and $i+1$, in a one-dimensional OFCR model. This is the situation after a main shock. In red we indicate the site thresholds. The blue dashed line represents the average stress $\overline{\sigma}$ of the three sites, while the blue arrows represent the effect of the relaxation on the system. As you may see, in this case the relaxation will bring the site i above threshold, so the site i will be the epicenter of the first aftershock.

This is a picture of the situation after a main shock, so all the blocks' stress is under threshold. Remember we are implementing this mechanism on the OFC* model, so every site of the example has its own threshold. With the blue arrows we represent the effect of the relaxation: as we said before, it tends to smoothen

the stress field, and it is possible that in the process it brings a new site above threshold. In the example the site i will be then the epicenter of a new event, the aftershock, generated without the drive but only through this mechanism.

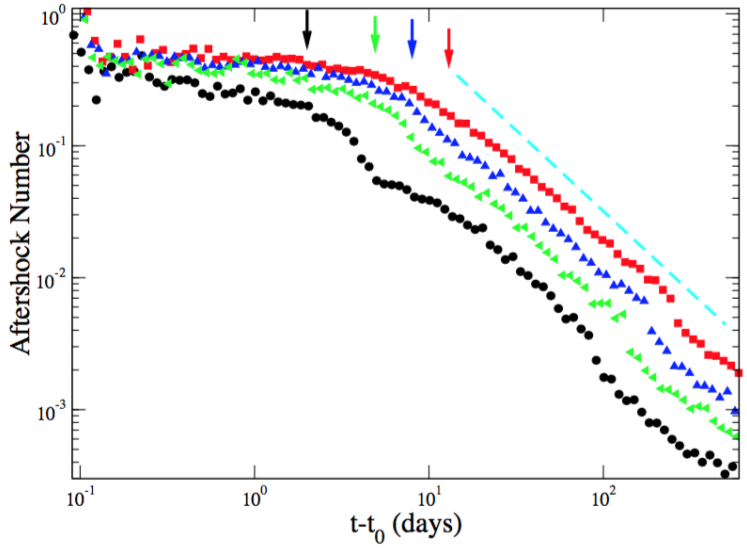

Figure 4.3: The temporal decay of the number of aftershocks after a mainshock with magnitude $m_M = 6.7$ in the OFCR model for a system of size $L = 1000$. Data exhibit different characteristic time scales c(indicated by colored vertical arrows) for the onset of the power law decay for different values of the initial shear stress (decreasing from left to right). The cyan dashed line indicates the Omori power law decay with an exponent p = 1.1 (From [54]).

In Fig.4.3 we plot the aftershock number as function of time from the main shock for the OFCR model, assuming different stress perturbations corresponding to different levels of stress in the system. We notice that all curves are in agreement with the experimental Omori law with an exponent $p \simeq 1.1$ and a characteristic time c that depends on the stress level. Interestingly, data indicate that c is a decreasing function of the stress level in agreement with experimental observations [76].

4.3 Viscous coupling in elastic interfaces model

A simple way to introduce relaxation in the OFC* model is represented by the model sketched in Fig.4.4. Due to its simplicity, the model allows for analytic treatment in mean field, and for extensive numerical simulations in finite dimensions [10].

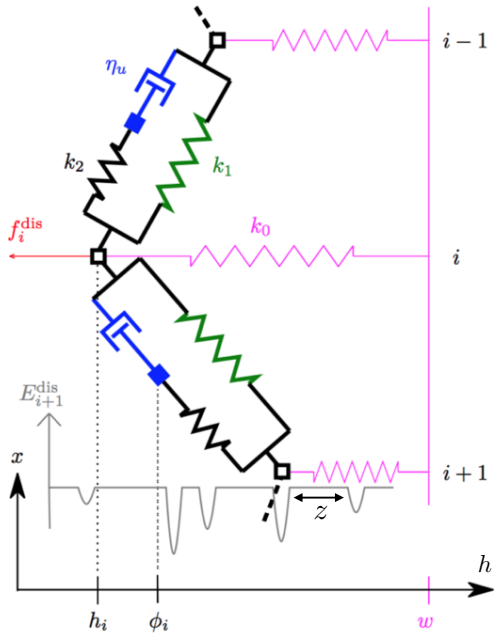

Figure 4.4: Mechanical sketch of the one-dimensional viscoelastic model. The interface (bold black line) consists in blocks located at discrete sites $i, i+1, ...$ (empty squares with location $h_i, h_{i+1}, ...$) along the x-axis and are connected via a combination of springs (k_1, k_2) and a dashpot (η_u). The additional (internal) degree of freedom ϕ_i is represented by a full square (blue). The driving is performed via springs k_0 linked to a common position w (thin purple lines). The disorder force f^{dis} (red) for the site i derives from a disordered energy potential E^{dis}, which is here simplified as a series of narrow wells separated by random spacings z (Adapted from [61]).

The interface is decomposed in blocks of mass m, labelled i and moving along the h-axes. As you may see, the original neighbor elastic interaction k_1 is a replaced

by a combination of springs (k_1, k_2) and a dashpot (η_u). ϕ is the position of the dashpot, which it is assumed with no mass. The action of the dashpot is to resist the change in $(\phi_i - h_i)$ via viscous friction, with a resulting force on h_i given by:

$$\eta_u \partial_t (\phi_i - h_i)$$

The blocks move in a medium with some effective viscosity η and we are interested in the overdamped regime, $m\partial_t^2 h_i \ll \eta \partial_t h_i$. As each block is described by two degrees of freedom h_i and ϕ_i, the time evolution is governed by two equations. Using the narrows wells representation for the disorder (see sec. 3.2), the equations read:

$$\eta \partial_t h_i = k_0(w - h_i) + f_i^{th} + k_1 \nabla^2 h_i + k_2(\nabla^2 h_i - u_i) \quad (4.2)$$

$$\eta_u \partial_t u_i = k_2(\nabla^2 h_i - u_i), \quad (4.3)$$

where the auxiliary variables u_i depend on the elongation of the neighboring dashpots: in one dimension this variable reads $u_i = (\phi_i - h_i) + (h_{i-1} - \phi_{i-1})$. The threshold force f_i^{th} has some random distribution (e.g. a Gaussian) and the narrow wells are separated by spacings z with some distribution $g(z)$ with finite average $\overline{z}$. The relaxation constant η_u sets a new time scale: $\tau_u = \eta_u / k_2$, which is characteristic of the relaxation of the dashpots (it corresponds to τ_R of the OFCR model). It can be compared with two other time scales: $\tau_D = \overline{z}/V_0$, which accounts for the slow increase of the external drive $w = V_0 t$, and τ_0, the response time of the position h of the blocks, i. e. the avalanche time scale. Assuming $\tau_0 \ll \tau_u \ll \tau_D$, the dynamics is the following:

- **Drive** all the blocks' stress is increased uniformly until a block becomes unstable and an avalanche starts;

- **Avalanche** the avalanche develops at a time scale $\tau_0 \ll \tau_u$, so in this stage the u_i are constants in time and the dynamics is exactly the same as in the depinning model with elastic constant $k_1 + k_2$;

- **Relaxation** the avalanche ends when no other site is unstable, so the h_i are all pinned; at the time scale $\tau_u > \tau_0$ the variable u_i starts to relax, according to:

$$u_i(t) = \nabla^2 h_i + (u_i(t_0) - \nabla^2 h_i) \exp(-(t - t_0)\frac{k_2}{\eta_u}),$$

where t_0 is the time at which the last avalanche occurred. The effect of relaxation is to reduce the term $k_2(\nabla^2 h_i - u_i)$ in Eq.4.2, until it is suppressed; during this process, or at the end of it some blocks may become unstable. This triggers secondary avalanches in the system, identified with aftershocks in the seismic context.

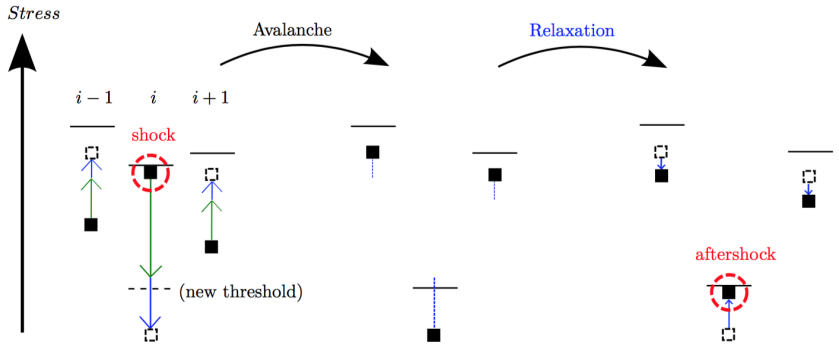

Figure 4.5: Schematic description of the evolution of the local stress σ_i over time for three sites (From [61]).

In Fig.4.5 we report a schematic illustration in one dimension of the effect of the relaxation on the system, in terms of the viscoelastic parameters.

- **Left panel**: the site i is at threshold: its stress will drop to zero, giving to the neighbors a pulse which depends on k_1 (elastic coupling), k_2 (the elastic parameter linked to the viscoelastic interaction) and on the value of the stress before the toppling (in this case σ_i^{th});

- **Central panel**: the situation after the toppling of the site i: a new threshold is drawn and the part of the stress drop due to the viscoelastic coupling

is remarked in blue;

- **Right panel** during the relaxation the part of the stress drop that depends on k_2 starts to diminish, and this mechanism eventually leads to an aftershock, even before that the relaxation is completed, as it happens in our example.

Numerical results [10] show that the avalanche size distribution, in the two-dimensional case, follows a power law with an exponent $\tau \sim 1.7$, the same exponent of the empirical GR law, as it happens in the OFCR model. In Fig.4.6 we report an example.

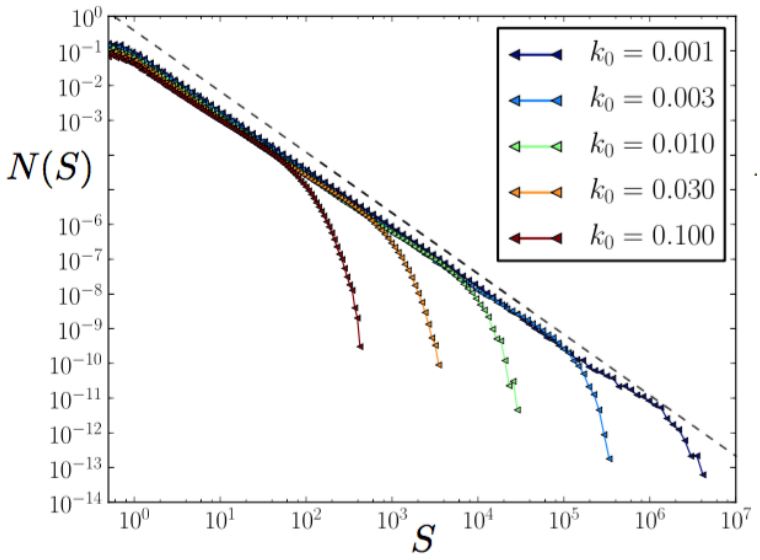

Figure 4.6: Number $N(S)$ of avalanches of size S for the 2-dimensional viscoelastic interface model, on a lattice of $5000x5000$ sites. The dashed lines indicate the pure power-law with exponent 1.75. The cut-off vanishes in the limit $k_0 \to 0$. (From [61])

The aftershocks distribution in time does not display, unlike the OFCR case, a power law behavior. It is possible to retrieve a power law behavior with a different

implementation of the relaxation mechanism, the Laplacian relaxation:

$$\eta_u \partial_t u_i = k_2(\nabla^2 h_i - \nabla^2 u_i),$$

but the exponent is still not the same as in the Omori law ($\tau \sim 2$).

Another interesting outcome of this model is the periodic or quasi-periodic behavior. In mean field, the relaxation of the viscoelastic elements generates a dynamical instability, responsible for the occurrence of periodic system-size events and macroscopic oscillations of the stress. The time scale of these oscillations is distinct from the microscopic time scale associated to the relaxation. Instead, the oscillations are characterized by a new, emerging time scale. The emergence of this cycle results from the competition between the slow viscoelastic relaxation and the fast avalanche dynamics: the slow dynamics drives the system towards a critical point unstable with respect to the fast avalanche dynamics. In two dimensions the global oscillations found in mean field disappear, but there are coherent oscillations of the local stress on finite regions of large sizes.

Chapter 5

Mean Field analysis of the OFC and OFC* model

In this Chapter we report our mean field analysis of the OFC model and some variations of its dynamics.

As we observed at the end of Chapter 3, the avalanche size distribution presents different features in the OFC and OFC* models; while in the first case we have a power law distribution with an exponent that changes with the dissipation parameter α, in the second one the power law exponent is stable, only the cut-off depends on α. In order to address these differences, we decided to perform a mean field analysis of the two models, with or without annealed disorder, and to focus our attention on the synchronization of the systems. By synchronization here we mean the possibility, for a group of blocks, to stay locked in the same avalanche under the dynamic evolution of the stress distribution. This mechanism was studied in systems consisting of globally coupled integrate-and-fire oscillators networks [69] [70], models very similar to our own. Moreover, Middleton and Tang [11] ascribed criticality of the OFC model to a mechanism of partial synchronization, induced by inhomogeneities from the boundaries. We want to check in mean field, where there is no underlying structure of the system, if this partial synchronization arise too and for which parameters values.

5.1 Fully connected model

In the following we generalize the OFC dynamics, introduced in the previous chapters, in a way that allows us to consider the OFC* and other variations, as a particular case of the general scheme. The fault is stylized as a system of N oscillators associated with a real state variable σ_i, representing the local stress. The total applied stress is given by:

$$\Sigma = \frac{1}{N}\sum_{i=1}^{N}\sigma_i.$$

The system is stable when all local stresses are below a pre-assigned threshold stress value, σ_i^{th}.

In the quasi-static approximation, dynamics consists of two well separated regimes: the drive and the avalanche.

- **Drive**: in the beginning all the state variables are below their thresholds: $\sigma_i(t) < \sigma_i^{th}$; they grow linearly in t until one of them reaches σ_i^{th}. Namely,

$$\sigma_i \to \sigma_i + \delta_{\min}, \qquad \forall i = 1, \cdots, N.$$

  where

$$\delta_{\min} = \min_{i\in[1,N]}(\sigma_i^{th} - \sigma_i)$$

- **Avalanche**: the value σ_i of the oscillator at or above threshold drops of a certain amount, giving to every oscillator, including itself, a pulse, according to the rules:

$$\sigma_i \to \sigma_i - (\widetilde{k}_1 + k_0)z \tag{5.1}$$
$$\sigma_j \to \sigma_j + \widetilde{k}_1 z/N \qquad \forall j = 1, \cdots, N. \tag{5.2}$$

  where $z > 0$ is a real number representing the displacement or *jump* of the oscillator's position, and k_0 and $\widetilde{k}_1$ are positive constants, representing the coupling of the oscillator, respectively, with the drive and with the other oscillators (for a 1-dim example see figure 2.1). We utilize the variable $\widetilde{k}_1 = Nk_1$ to keep the pulse intensive in N. The total applied stress drops of an

amount $k_0 z$, hence $k_0 z$ controls the amount of dissipation. The pulse given by the oscillator can destabilize other oscillators that are close enough to their own threshold. These oscillators can be also activated if $\sigma_i \geq \sigma_i^{th}$. The *avalanche* ends when no other pulse is sufficient to bring any other oscillator above threshold. At this point the drive-process starts again.

It is possible to define the *size* of an avalanche either as the total number of sites who has been activated or as the total displacement $\sum z_i$. In the following we will consider the first definition.

In the quasi-static regime avalanches are assumed to be instantaneous compared to the drive. In the following we will discuss four different cases:

- the **Uniform threshold and Jump to Zero** case: we assume

$$\sigma_j^{th} = 1, \qquad \forall j$$

and

$$z = \frac{\sigma_i}{\widetilde{k}_1 + k_0}, \qquad \forall j,$$

where σ_i is the value of stress immediately before destabilization.
This means that the local stress of the unstable sites jumps to zero because of the slip. This case corresponds to the standard OFC model.

- the **Uniform Threshold and Fixed Jump** case: we assume

$$\sigma_j^{th} = 1, \qquad \forall j$$

and

$$z = \frac{1}{\widetilde{k}_1 + k_0}, \qquad \forall j.$$

This means that all unstable sites slip of the same amount and their stress drops from σ_i to $\sigma_i - 1$. This case in two dimensions corresponds to the generalized BTW model we discussed in sec. 2.3.2.

- the **Uniform Threshold and Random Jump** case: we assume

$$\sigma_j^{th} = 1, \qquad \forall j$$

and z is drawn from a random distribution $g(z)$, and updated each time an oscillator topples. We use the exponential distribution since, as we mentioned before, it implies a more realistic pattern of irregularities in the system. This case corresponds to a variant of the OFC* model [65].

- the **Random Threshold and Random Jump** case: we implement disorder also in the thresholds, and we update the threshold value σ_i^{th} after every instability. This model corresponds to the OFC* model [65].

5.1.1 Synchronization mechanism

We better clarify our definition of synchronization. Two oscillators σ_i and σ_j are synchronized if, when σ_i is unstable, the pulse q transferred to the others brings σ_j above threshold as well. This way the two oscillators are locked in the same avalanche. In the study of synchronization we adopt the following notation: given a certain avalanche, the site index $i(n)$ indicates the index of the site that performs the n-th toppling during the avalanche. For example, if the site $i = 4$ is the epicenter of a new event, we have $\sigma_{i(1)} = \sigma_4$.

The locking condition then reads:

$$\sigma_{i(n)} - \sigma_{i(n+1)} \leq q(n), \tag{5.3}$$

where we considered the fact that the pulse $q(n)$ can depend on $\sigma_{i(n)}$, i.e. the value of the first oscillator before the toppling. This condition can be generalized to the situation where two oscillators don't topple one after another, but still in the same avalanche; in this case the site $i(m)$ receive $(m - n)$ pulses from all the oscillators that toppled before it $(n < m)$, leading to the locking condition:

$$\sigma_{i(n)} - \sigma_{i(m)} \leq \sum_{k=n}^{m-1} q(k). \tag{5.4}$$

In order to study how this mechanism affects our systems' criticality, we will check how the stress differences between oscillators evolve during the dynamics.

5.2 Fixed Threshold and Jump to Zero

5.2.1 Synchronization

This is the case of the standard OFC model. The locking condition between two oscillators that topples one after another here reads:

$$\sigma_{i(n)} - \sigma_{i(n+1)} \leq \widetilde{k}_1 \frac{z}{N} = \frac{\widetilde{k}_1}{(\widetilde{k}_1 + k_0)N} \sigma_{i(n)},$$

where $\sigma_i(n)$ is the stress of the oscillator that performs the n-toppling, just before he topples. In order to enlighten the $\sigma_{i(n)}$-dependence, we rewrite the locking condition as:

$$\sigma_{i(n)} - \sigma_{i(n+1)} \leq q\sigma_{i(n)},$$

with

$$q = \frac{\widetilde{k}_1}{(\widetilde{k}_1 + k_0)N}.$$

Notice that, if we do the substitution ($\widetilde{k}_1 \to k_1 N$), we retrieve $q = \alpha$. The generic locking condition between two oscillators then is:

$$\sigma_{i(n)} - \sigma_{i(m)} \leq q \sum_{k=n}^{m-1} \sigma_{i(k)}$$

Therefore the avalanche dynamics evolves according to the rules:

$$\begin{aligned} \sigma_i &\to q\sigma_i \\ \sigma_j &\to \sigma_j + q\sigma_i \qquad \forall j \neq i, \end{aligned}$$

remembering that the oscillator that topples gives a pulse also to itself.

Aiming to check the effect of the dynamics on the gap, we consider as an

example three oscillators locked in the first avalanche:

$$\sigma_{i(1)} = 1, \quad \sigma_{i(2)} = 1 - q + \epsilon_1 > \sigma_{i(3)} = 1 - q + \epsilon_2$$

In Table 5.1 we reported the evolution of their stress under the OFC dynamical rules.

	Drive	**First T.**	**Second T.**	**Third T.**
$\sigma_{i(1)} \rightarrow$	1	q	$q + q(1 + \epsilon_1)$	$q + q(1 + \epsilon_1) + q(1 + \epsilon_2 + q(1 + \epsilon_1))$
$\sigma_{i(2)} \rightarrow$	$1 - q + \epsilon_1$	$1 + \epsilon_1$	$q(1 + \epsilon_1)$	$q(1 + \epsilon_1) + q(1 + \epsilon_2 + q(1 + \epsilon_1))$
$\sigma_{i(3)} \rightarrow$	$1 - q + \epsilon_2$	$1 + \epsilon_2$	$1 + \epsilon_2 + q(1 + \epsilon_1)$	$q(1 + \epsilon_2 + q(1 + \epsilon_1))$

Table 5.1: Evolution of the stress during an avalanche (jump to zero rule).

The avalanche does change the gap between oscillators, making it dependent on the stress value of the oscillator just before the toppling:

$$\sigma^A_{i(n)} - \sigma^A_{i(n+1)} = q\sigma'_{i(n)},$$

where with σ^A_i we indicate the value of the oscillator's stress after the avalanche, and with σ'_i the value just before the toppling.

In our example the gaps are changed in the following way (σ^B_i corresponds to the value before the avalanche):

$$\begin{aligned} \sigma^B_{i(1)} - \sigma^B_{i(2)} &= q - \epsilon_1 \qquad & \sigma^A_{i(1)} - \sigma^A_{i(2)} &= q \\ \sigma^B_{i(1)} - \sigma^B_{i(3)} &= q - \epsilon_2 \qquad & \sigma^A_{i(1)} - \sigma^A_{i(3)} &= q + q(1 + \epsilon_1) \end{aligned}$$

It is then evident that, in a new avalanche, after the toppling of $i(2)$, the gap $\sigma_{i(1)} - \sigma_{i(3)}$ does not satisfy the locking condition anymore:

$$\sigma^A_{i(1)} - \sigma^A_{i(3)} = 2q + q\epsilon_1 > 2q$$

and therefore this kind of dynamics decouples oscillators' locking. In fact the presence of upper-critical sites enlarges the gaps, the synchronization is annealed and, after a transient (due to the initial condition), a regime of avalanches of size 1 or 2 is reached.

5.3 Uniform Threshold and Fixed Jump

5.3.1 Synchronization

In the case of fixed jump, since $z = \frac{1}{\widetilde{k}_1 + k_0}$, we have:

$$\sigma_{i(n)} - \sigma_{i(n+1)} \leq q(n) = q,$$

where:

$$q = \frac{\widetilde{k}_1}{(\widetilde{k}_1 + k_0)N}.$$

As you may see, the pulse in this case is independent of the stress value $\sigma_{i(n)}$ and it is a constant. The oscillator i above threshold, hence, topples and gives a pulse to any other oscillator, including itself, according to the rule:

$$\sigma_i \rightarrow \sigma_i - 1 + q \tag{5.5}$$

$$\sigma_j \rightarrow \sigma_j + q \qquad \forall j \neq i \tag{5.6}$$

We identify again as σ_i^B and σ_i^A, respectively, the value of the stress of the i-th oscillator immediately before and after an avalanche. It is easy to see that, applying the Eq.5.5 and Eq.5.6 to the first member of the locking condition, we obtain:

$$\sigma^A_{i(n)} - \sigma^A_{i(n+1)} = \sigma^B_{i(n)} - \sigma^B_{i(n+1)}.$$

As an example, let us consider the evolution of three oscillators ($i = 1, 2, 3$) involved in the same avalanche. The evolution under this dynamics is reported in Table 5.2.

	Drive	**First Toppling**	**Second Toppling**	**Third Toppling**
$\sigma_{i(1)} \rightarrow$	$\sigma_{i(1)} + \Delta$	$\sigma_{i(1)} + \Delta - 1 + q$	$\sigma_{i(1)} + \Delta - 1 + 2q$	$\sigma_{i(1)} + \Delta - 1 + 3q$
$\sigma_{i(2)} \rightarrow$	$\sigma_{i(2)} + \Delta$	$\sigma_{i(2)} + \Delta + q$	$\sigma_{i(2)} + \Delta + q - 1 + q$	$\sigma_{i(2)} + \Delta + q - 1 + 2q$
$\sigma_{i(3)} \rightarrow$	$\sigma_{i(3)} + \Delta$	$\sigma_{i(3)} + \Delta + q$	$\sigma_{i(3)} + \Delta + 2q$	$\sigma_{i(3)} + \Delta + 2q - 1 + q$

Table 5.2: Evolution of the stress during an avalanche (fixed jump rule).

Hence, the oscillators locked in an avalanche will remain locked also in the next one. This means that the avalanche does not influence the locking, and the order

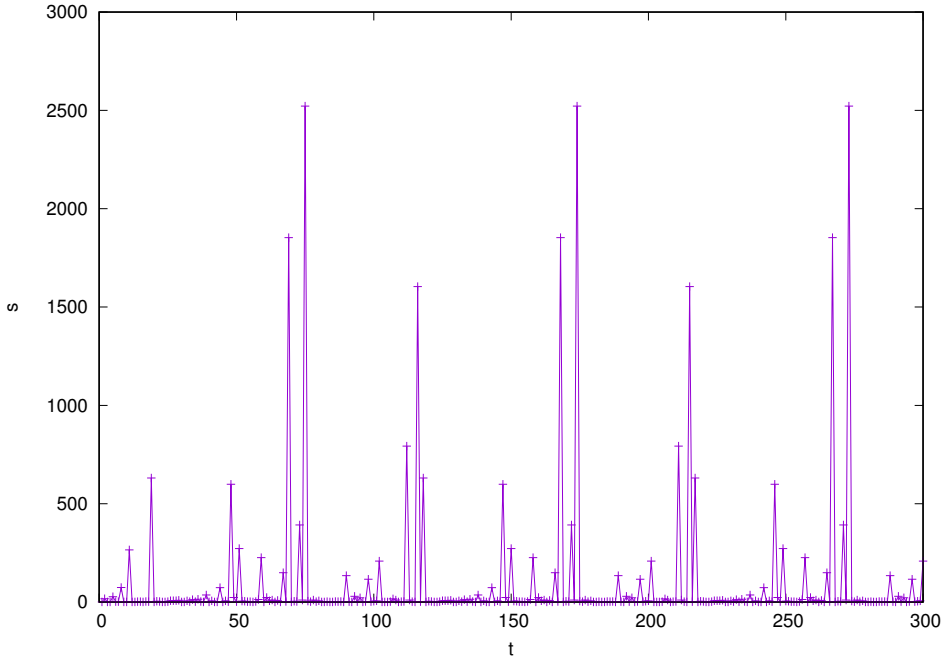

Figure 5.1: This is a sequence of avalanches in time (s represents the size of the avalanche, t the time in drive units) in case of fixed threshold and fixed jump, for a system of $N = 10^4$ oscillators with random initial conditions and for the parameters: $\widetilde{k}_1 = 0.01N$ and $k_0 = 1$. This sequence repeats itself after a period of 99 time steps.

of topplings will remain unchanged. We can conclude that, in the case of the fixed jump scenario, once the oscillators are locked in an avalanche they will stay locked in the following ones. As a consequence the dynamics here, after a transient, is periodic (see an example in figure 5.1), with the *period* given by the time after which all the oscillators are activated at least one time.

The explanation of the initial transient regime is reported in Fig.5.2. Violet circles are the sites involved in the first avalanche, green circles the sites involved in the second one while red circles are the group closest to zero, because of the random initial condition. After the violet group performs the first avalanche ($0 < t < T$), they will be the new group closest to zero and it is possible that their stress gap with the first one of the red group fits the locking condition; after the second avalanche, performed by the green circles, it is possible that this happens again

because the fact that they did not fulfill the locking condition with the violet group does not imply that they can not be locked to the red group; when this red group finally arrives at the threshold ($t = T$), it will bring with him in the same avalanche also these new oscillators. This effect will end when a cycle is finished, i.e. when all the oscillators toppled at least one time. After that, as we previously pointed out, the dynamics does not change the gap arrangement between the oscillators, implying that we will see always the same avalanches (periodicity).

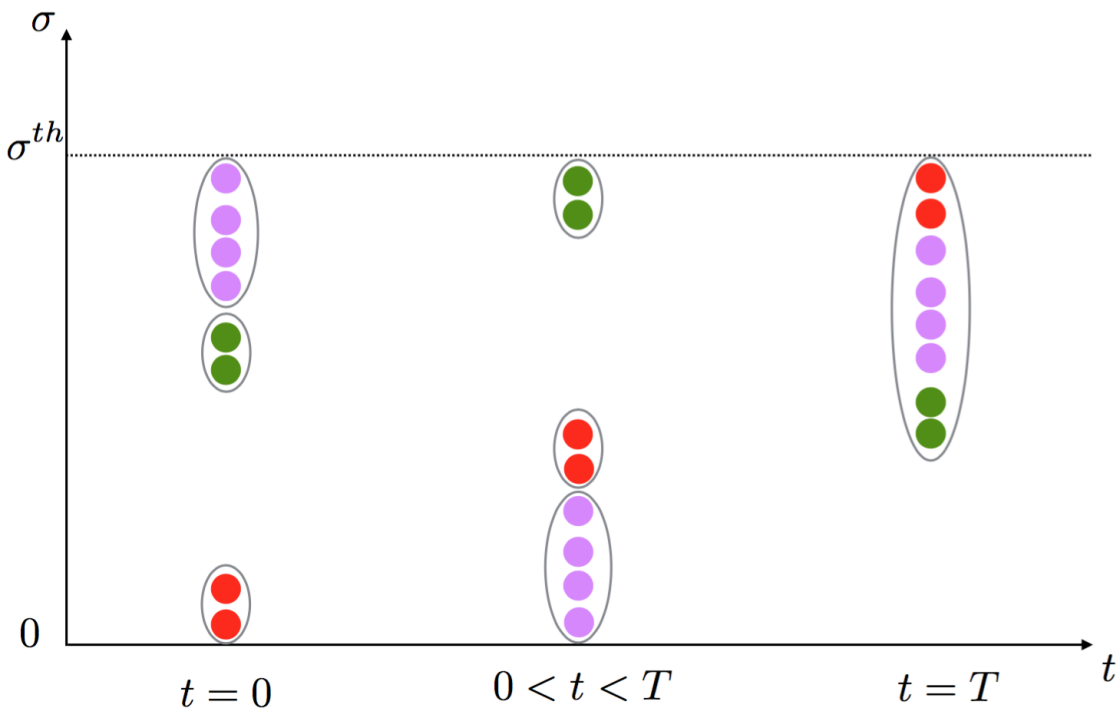

Figure 5.2: An example of a possible initial condition leading to a rearrangement of the oscillators' locking after a first cycle; as you may see, the oscillators that belong to three different avalanches for $t = 0$, are the same that, after the first cycle, belong to a single avalanche.

5.3.2 Size distribution and percolative analysis of the distribution of the gaps

We performed numerical simulations of a system of $N = 10^4$ sites, keeping $k_0 = 1$ and varying $\widetilde{k}_1$. For the avalanche size distribution we obtained three regimes, as you may see in Fig.5.3:

- **Subcritical** $q < 0.99/N$: the avalanches size never reach the system size, but it has a short cut-off s_m;

- **Critical** $q \simeq 0.99/N$: the distribution reach the size of the system and is a power law with an exponent $\tau \simeq 1.5$;

- **Upper critical** $q > 0.99/N$: it appears a bump in the distribution at the system size, indicating a tendence to the system to develop an infinite avalanche.

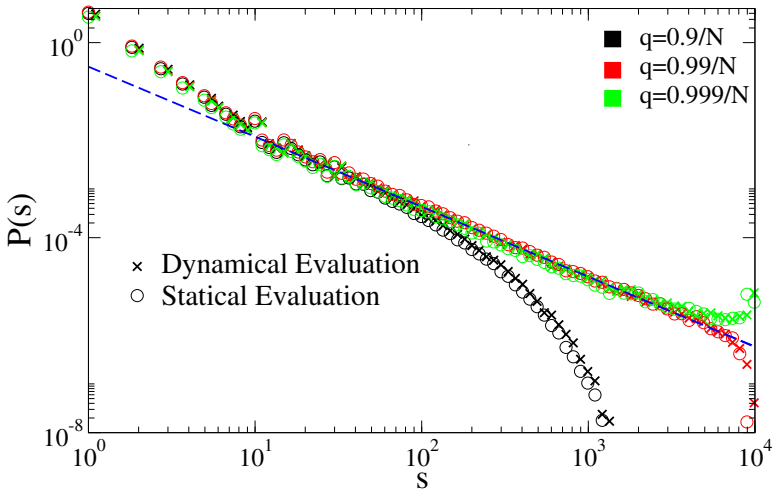

Figure 5.3: Avalanche size distribution (crosses) and gap cluster size distribution (circles) for three different values of the elastic coupling. The dashed blue line is the power law $s^{-\tau}$. In both cases we considered a system $N = 10^4$ oscillators. We observe a critical behavior (dashed blue line) with the same exponent $\tau = 1.5$ for the value $q = 0.99/N$.

The behavior of the cut-off s_m with the distance from the conservative limit $q_c = 1/N$ is reported in Fig.5.4. The cut-off follows a power law behavior with an exponent $a \sim 2$ for q values far enough from q_c. As q approaches q_c the behavior is lost because of finite size effects.

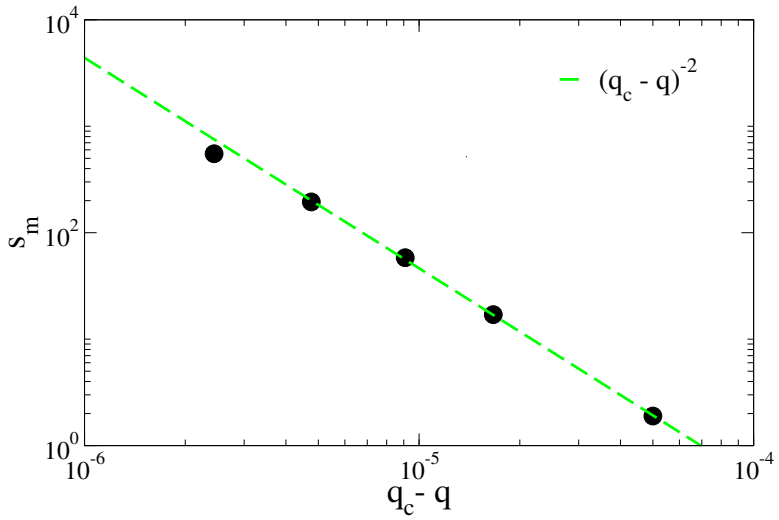

Figure 5.4: The cut-off of the avalanche size distribution as a function of the distance from the critical point; the green dashed line represents the power law behavior of s_m with an exponent 2.

Since in this system, after a first cycle of avalanches, the gaps between oscillators' stress are unaltered by the dynamics, the avalanche size distribution can be directly extracted from the organization of the gaps.

We start from random initial conditions with the stress values of the N oscillators drawn from an uniform distribution between 0 and 1 (our threshold). As a result, the probability distribution of the gaps ($\Delta\sigma_i = \sigma_{i-1} - \sigma_i$) is an exponential distribution, namely:

$$p(\Delta\sigma) = Ne^{-N\Delta\sigma}.$$

Note that here we are considering the oscillators ordered by decreasing stress value ($\sigma_1 > \sigma_2 > \cdots > \sigma_N$).

We want to evaluate the probability to have an avalanche of size k. In order

to do that we introduce the variable:

$$S_n = \Delta\sigma_1 + \cdots + \Delta\sigma_n = \sigma_1 - \sigma_n$$

Since all the members of this sum are independent random variables identically distributed, with an exponential distribution, S_n is an Erlang variable [72], and its probability density and cumulative distribution therefore are:

$$\begin{aligned} p(S_n) &= N\frac{(NS_n)^{n-1}}{(n-1)!}e^{-NS_n} \\ P(S_n \leq x) &= 1 - e^{-Nx}\Big(1 + \frac{Nx}{1!} + \cdots + \frac{(Nx)^{(n-1)}}{(n-1)!}\Big). \end{aligned}$$

Starting from $\sigma_1 = \sigma_{th}$, the probability to have an avalanche of size k will be given by the product of the probability that the first k oscillators are locked in the avalanche, and the probability that the $(k+1)$-th is not. Then:

$$\begin{aligned} P_{cluster}(k) &= \prod_{i=1}^{k} P(S_i \leq iq) \cdot P(S_{k+1} > (k+1)q) \\ &= \prod_{i=1}^{k} \Big[1 - e^{-Niq}\Big(1 + \sum_{j=1}^{i-1}\frac{(Niq)^j}{j!}\Big)\Big] \cdot e^{-N(k+1)q}\Big(1 + \sum_{j=1}^{k}\frac{[N(k+1)q]^j}{j!}\Big) \end{aligned}$$

This quantity is difficult to compute analytically, so in Fig.5.3 we report a numerical evaluation of the distribution of the gaps cluster size, for different values of $\widetilde{k}_1$ (or q). From the comparison in Fig.5.3 it is clear that the behavior is the same, both distributed on a power law with the same exponent $\tau = 1.5$, once the parameter $\widetilde{k}_1$ has reached the value $\widetilde{k}_1 = 0.01N$.

5.3.3 Map to the Problem of First-Crossing

We said that an avalanche of size s corresponds to the first time the relation:

$$S_{k-1} \leq qs < S_k$$

is fulfilled. Because of the fact that the variables $\Delta\sigma_i$ are independent variables identically distributed, with exponential distribution, it is possible to identify the sequence $\Delta\sigma_1, \ldots, \Delta\sigma_n$ as a random walk, with diffusion constant: $D = 1/N$ and drift $d = 1/N$. When it crosses the line of slope q, the avalanche is over. In Fig.5.5 we report a sketch representing the situation. The statistics for the avalanche size

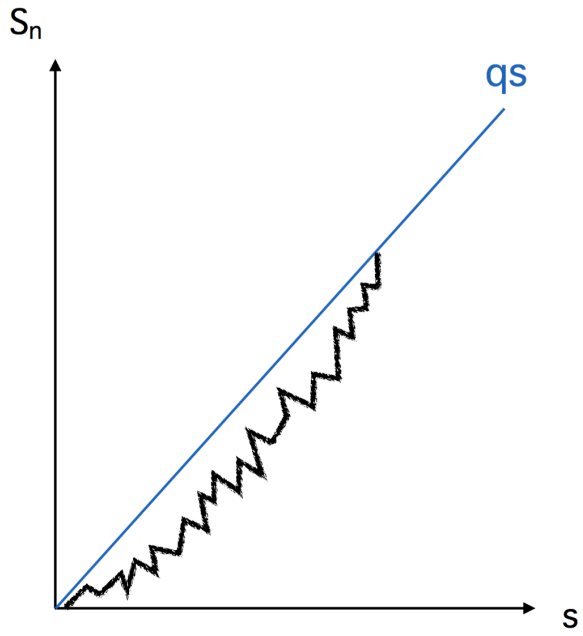

Figure 5.5: A schematic representation of the locking condition: in black the brownian motion corresponding to the path S_n, i.e. the sum of all the gaps between the oscillators; in blue the killing wall $S_n = qs$. The first value s for which the BM crosses the killing wall corresponds to the size of the avalanche.

thus is the same as for a problem of first zero crossing of a random walk with diffusion constant $D = 1/N$ and drift $d = q - 1/N$. For a positive drift, there is a finite probability that this random walk never crosses zero, which corresponds to an infinite avalanche. For a negative drift, the time of zero crossing is always finite, and has been computed for the Brownian motion in [68]. The distribution of the avalanche sizes thus reads:

$$N(s) \sim s^{-3/2} e^{-s/2s_m} \tag{5.7}$$

with

$$s_m = \frac{D}{d^2} \propto \Big(\frac{k_0 + \widetilde{k}_1}{k_0}\Big)^2.$$

These results are consistent with our result, as:

$$s_m \propto (q_c - q)^{-2} = \Big(\frac{1}{N} - \frac{1}{N}\frac{\widetilde{k}_1}{\widetilde{k}_1 + k_0}\Big)^{-2} = \Big(\frac{1}{N}\frac{k_0}{\widetilde{k}_1 + k_0}\Big)^{-2}.$$

5.4 Fixed Threshold and Random Jump

5.4.1 Synchronization

This case corresponds to the modified OFC* model that we discussed at the end of Chapter 3. The locking condition of Eq.5.4 reads:

$$\sigma_{i(n)} - \sigma_{i(m)} \leq \frac{\widetilde{k}_1}{N} \sum_{j=n}^{m-1} z_j,$$

where the position jumps z_j are drawn each time from a random distribution $g(z)$. In the following we will consider the exponential distribution, for the reasons already illustrated in the description of the original OFC* model.

Unlike the previous cases, here it is no longer possible to follow the stress gaps during an hypothetical avalanche, since the jump, and as a consequence the pulse, is totally random. If we look at a sequence of avalanches over time, though, we immediately see that there is no longer a periodic structure. Moreover, it it possible to refer to an averaged locking condition, as we will see shortly.

5.4.2 Size distribution

In Fig.5.6 we report the numerical results for the avalanche size distribution. Again we have three regimes: a subcritical one, with an exponential cut-off that depends on the distance to criticality; a critical one, with a power law behavior for the critical value $\widetilde{k}_1 = 10^{-2}N$ (which corresponds to one of the previous case $q = 0.99/N$); an Upper critical critical one with the occurrence of a bump on the system size which is a finite size effect. Interestingly, we retrieve the same critical exponent

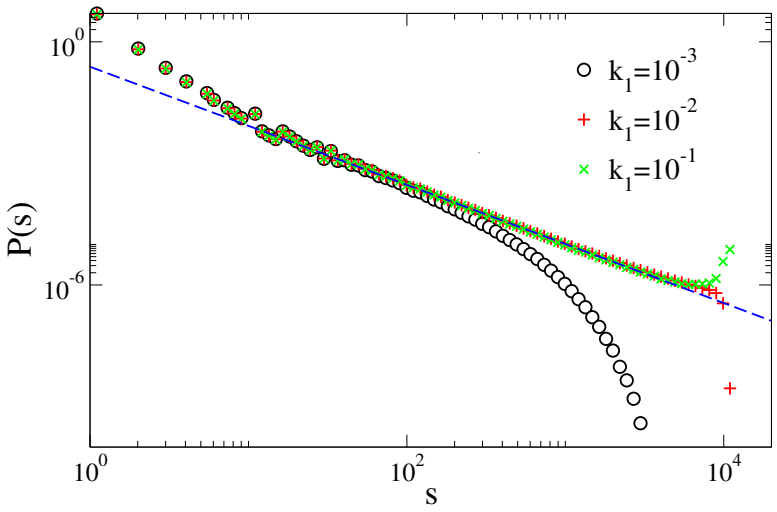

Figure 5.6: Avalanche size distribution for a system of $N = 10^4$ oscillators. The dashed blue line represents the power law $s^{-\tau}$, with $\tau \simeq 1.5$.

$\tau \simeq 1.5$ as before. In Fig.5.7 there is a comparison of the two distributions for the three regimes we considered. The behavior is exactly the same, with a slightly

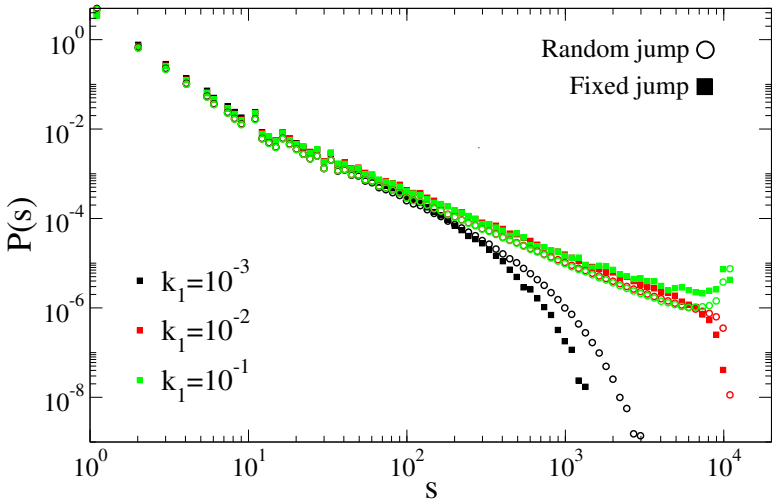

Figure 5.7: A comparison of the avalanche size distribution for the two models we discussed, fixed jump (circles) and random jump (squares) for the three regimes we found.

different cut off in the subcritical regime. Despite that, s_m is again a quadratic

function of the distance from the conservative point, as the reader may check in Fig.5.8, where we plotted the cut-off as a function of the quantity

$$q_c - q = \frac{k_0}{N(\widetilde{k}_1 + k_0)}$$

(we considered the q of the fixed jump case).

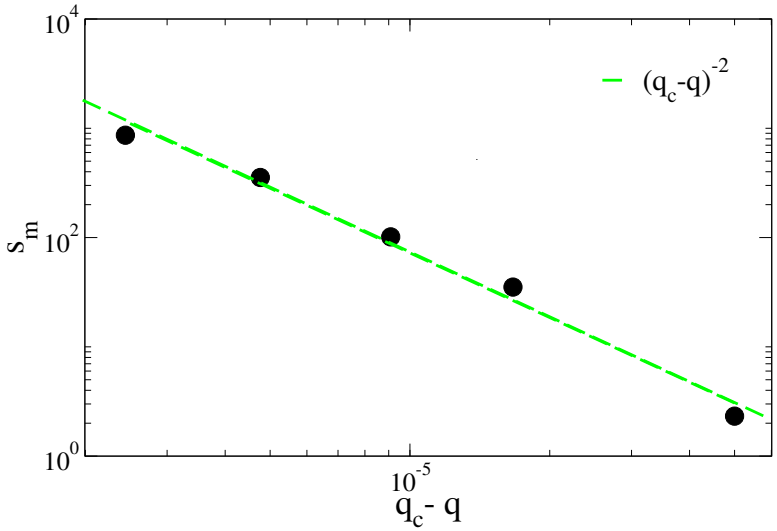

Figure 5.8: The cut-off of the avalanche size distribution as a function of the distance from the critical point; the green dashed line represents the power law behavior of s_m with an exponent 2. Here $q = \frac{\widetilde{k}_1}{(\widetilde{k}_1+k_0)N}$.

5.4.3 Map to the problem of first crossing

In the previous section we have seen that an avalanche of size s corresponds to the first time the condition

$$S_{k-1} \leq qs < S_k$$

verifies. There

$$q = \frac{\widetilde{k}_1}{N} z$$

was a constant, being the jump $z = 1/(\widetilde{k}_1 + k_0)$.

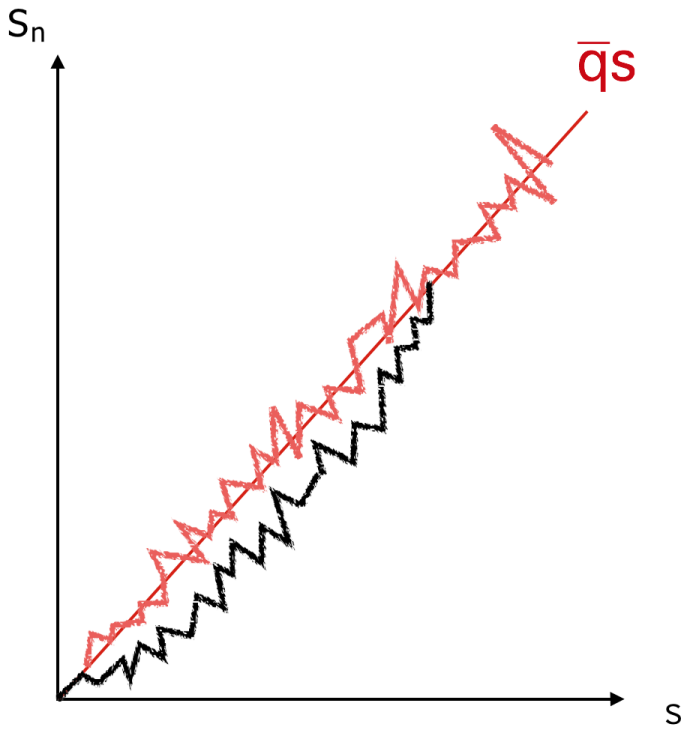

Figure 5.9: A schematic representation of the locking condition: in black the brownian motion corresponding to the path S_n, i.e. the sum of all the gaps between the oscillators; in red the Brownian Motion that represents the new killing wall, oscillating around the average $S_n = \overline{q}s$. The first value s for which the BM crosses the killing wall corresponds to the size of the avalanche.

In this case the jump is random, but we can look at the fixed value of the previous case as the average value $\overline{z}$ of a random distribution $g(z) = \delta(z - \overline{z})$. Then in case of the random jump, an avalanche of size s corresponds to the first time it is verified:

$$S_{k-1} \leq \overline{q}s < S_k,$$

where now $\overline{q} = \widetilde{k}_1\overline{z}/N$ corresponds to the average of a broader distribution. Following the reasoning of Sec.4.3.3., this problem can be mapped onto the first passage of a Brownian motion [61]. The only difference is that now the killing wall is no longer a straight line qs, but a brownian motion itself with finite average $\overline{q}s$.

Then the Eq.5.7 holds also in this case, where:

$$s_m = \frac{D}{d^2} \propto (1 - \overline{z}\widetilde{k}_1)^{-2}$$

5.5 Random Threshold and Random Jump

Finally, we analyzed the case that in 2 dimensions corresponds to the original OFC* model. As in the previous case, it is not possible to follow the evolution of the stress gaps during an avalanche. Moreover, since the quenched randomness is extended also to the thresholds, there are difficulties in the very same definition of the locking condition.

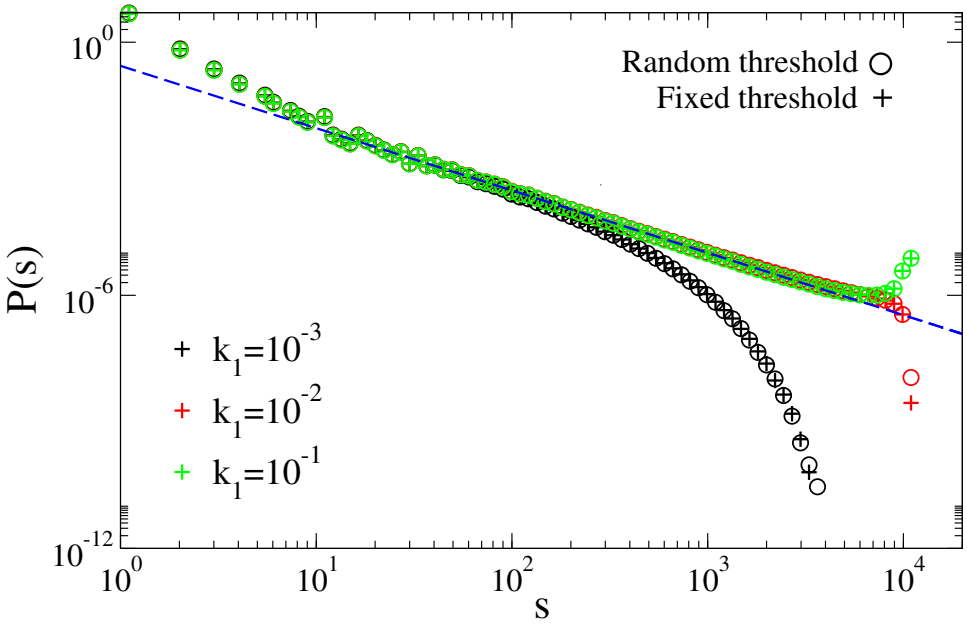

Figure 5.10: Avalanche size distributions in the case of random jump and: 1) fixed thresholds (plus) 2) random thresholds (circle), for the three different regimes. We simulated a system of $N = 10^4$ sites and the random distribution we utilized are the exponential one for the jumps, and the gaussian with mean 1 and deviation 0.8 for the thresholds. The blue dashed line indicate the power law behavior $s^{-\tau}$, with $\tau \simeq 1.5$.

We performed numerical simulations for different implementation of the dis-

order in the thresholds (exponential distribution and gaussian distribution) and in Fig.5.10 we report a comparison among the avalanche size distributions we obtained in this case and those obtained in the case of fixed threshold and random jump. There is a perfect correspondence between the two cases in all the regimes; even in the subcritical region the cut-off are exactly the same, despite the fact that in two dimensions they have different values (cfr Fig.3.4).

5.6 Mean field approach to the elastic interfaces problem

As a reference, we report analytical results for the elastic interface model in a disordered medium in the mean field approximation. We will consider a fully connected model where every point of the interface interact with all the others. With infinite range, the elastic interaction for i reads:

$$F_{el,i} = \frac{\widetilde{k}_1}{N} \sum_{j \neq i} (h_j - h_i),$$

where we must divide by the total number of sites N to keep the system's energy extensive in N. The sum can be rewritten as:

$$\sum_{j \neq i} (h_j - h_i) = \sum_j h_j - \sum_j h_i = N(\overline{h} - h_i).$$

As a consequence, the equation for h_i motion will be:

$$\eta \partial_t h_i = k_0(w - h_i) + \widetilde{k}_1(\overline{h} - h_i) - f_i^{dis}. \tag{5.8}$$

Summing Eq.5.8 over i and dividing it for the number of sites N we obtain the equation of motion for average displacement, equivalent of the center of mass of the interface:

$$\eta \partial_t \overline{h} = k_0(w - \overline{h}) - \frac{1}{N} \sum_i f_i^{dis}, \tag{5.9}$$

where the elastic terms cancelled each other. Since f_i^{dis} are independent random variables, for the central limit theorem the dynamics of the center of mass in the fully connected model can be mapped to the study of a single particle in an effective disordered potential [66]:

$$\eta \partial_t \overline{h} = k_0(w - \overline{h}) - \frac{1}{\sqrt{N}} \zeta(\overline{h}(t)); \tag{5.10}$$

here $\zeta(t)$ is a Brownian Motion process with finite variance, linked to the distribution of f_i^{dis}. The problem of a single particle driven in a Brownian force landscape [60] can be reformulated in terms of first crossing of a random walk with a line. In the quasi-static limit ($w = 0^+$) the Eq.5.10 can be seen in the following way:

- if $\sqrt{N} k_0(w - \overline{h}) < \zeta(\overline{h})$ the particle does not move;

- as soon as the equality is fulfilled, under the increasing of w, the particle starts moving of a distance s,

- it will keep moving as long as $\sqrt{N} k_0(w - \overline{h} - s) > \zeta(\overline{h} + s)$;

- the avalanche stops as soon as the equality is again verified.

Under an appropriate change of variables and a translation, the avalanche stopping condition reduces to:

$$\zeta(s) = -k_0 s,$$

meaning that the avalanche size s is distributed as the time of first crossing of a Brownian motion with the line of slope $-k_0$.

In the limit $k_0 \to 0$, the problem reduces to that of the return at the origin for a Brownian walker starting in zero. This distribution decays as:

$$P(s) \propto s^{-\frac{3}{2}},$$

so that the average size diverges. For finite k_0, the distribution has a cut-off at large length scales, which can be qualitative evaluated confronting the extension of

the killing wall $-k_0 s$, and the length of the free brownian motion $\sim s^{\frac{1}{2}}$. The typical size at which these two intersect is $s_m \sim k_0^{-2}$. So the probability distribution at finite k_0 reads:

$$P(s) \sim s^{-\frac{3}{2}} \exp\Big(-\frac{s}{4s_m}\Big), \quad \text{where} \tag{5.11}$$

$$\langle s \rangle \sim s_m^{\frac{1}{2}}. \tag{5.12}$$

For an exact computation the reader may check [67].

Considering that the mean field dimension corresponds to the upper critical one, which is $d_{uc} = 4$ [64], it is sufficient to inject $d = 4$ in the previous results in Eq.3.4, Eq.3.6 and Eq.3.7 to find:

$$\tau = 2 - 2/d = 3/2, \qquad s_m \sim \xi^4 \sim (k_0^{-1/2})^4, \qquad \langle s \rangle \sim 1/k_0,$$

proving the consistency of the finite dimension model with the fully connected one.

Chapter 6

Relaxation and the two blocks model: an analytical study

In this Chapter we report our analytical study of the effect of viscosity on the OFC dynamics, focusing on synchronization.

The emergence of a collective periodic behavior is a widespread phenomenon occurring in different fields, like in physics and engineering (arrays of lasers [12], charged density waves [13] [14], superconducting Josephson junctions [15]) or in biology (synchronously flashing fireflies [16], crickets that chirp in unison [17], cells of the heart pacemaker [18], circadian neural networks [19], metabolic synchrony in yeast cell suspensions [20]). The usual way to model these systems is by a set of oscillators that get locked in phase to each other because of global couplings. In particular, when the components of the system interact through the sudden firing of a pulse (e.g. fireflies communicating through light flashes, crickets exchanging chirps, neurons receiving and sending synaptic pulses) we can represent them as a system of integrate-and-fire oscillators which are described by a real state variable monotonically increasing up to a threshold. When this threshold is reached the oscillator comes back to the basic level (toppling) of the variable by firing a pulse to the other oscillators, eventually leading to an avalanche of topplings. Once all the oscillators topple another period begins. It was shown that such a system, in case of identical oscillators, can display global synchronization in a finite time. Our OFC model corresponds to this dynamics, with the only difference being the

nearest neighbor coupling instead of the global one. As we will see in detail later, Middleton and Tang [11] suggested that the introduction of inhomogeneities in the OFC dynamics, can induce synchronization and then criticality.

In order to address the role of the new mechanism of relaxation in the synchronization of the system, we will study the implementation of this mechanism in a simple OFC model made of two oscillators.

6.1 The model

We consider two oscillators associated with a real state variable σ_i, representing the local stress. The applied stress on the two oscillators system is given by:

$$\Sigma(t) = \sigma_1(t) + \sigma_2(t).$$

The system is stable when all local stress are below a threshold value, $\sigma^{th} = 1$. In the quasi-static approximation, the OFC dynamics consists of two well separated regimes: the drive and the avalanche.

- **Drive**: $\sigma_1(t)$ and $\sigma_2(t)$ grow linearly in t until one of them reaches σ^{th}. Namely,

$$\begin{aligned} &\sigma_i \to \sigma_i + \delta_{\min}, \quad \text{where} \\ &\delta_{\min} = \min\left(1 - \sigma_1, 1 - \sigma_2\right) \end{aligned}$$

- **Avalanche**: the value σ_i of the oscillator above threshold drops of an amount $(k_1/2 + k_0)z$ and gives to the oscillator a pulse $k_1 z/2$, according to the rules:

$$\sigma_i \to \sigma_i - (k_1 + k_0)z \tag{6.1}$$

$$\sigma_{j\neq i} \to \sigma_j + k_1 z \tag{6.2}$$

  where k_0 and k_1 are positive constants. Two particular cases can be discussed:

  - The jump to zero case corresponds to the case: $\sigma_i \to 0$. In this model

the dissipation is given by $1-\alpha = k_0/(k_1+k_0)$ and the randomness is provided by the initial condition only. This case corresponds to the standard OFC model.

– The random exponential jump where z is drawn from a distribution $g(z)$, and $g(z) = \exp(-z)$. This case corresponds to the OFC* model.

The solution of the two oscillator system is provided by the Poincaré map. We introduce the variable n as the index of the toppling of the oscillator 2. $\sigma_1(n)$ is therefore the local stress of the first oscillator right after the n^{th} toppling of the second oscillator. The Poincaré map evaluates the value $\sigma_1(n+1)$ as a function of $\sigma_1(n)$.

6.2 Jump to zero case: the periodic attractor

We assume that $\sigma_1(t=0) \geq 0$, $\sigma_2(t=0) = 0$. This implies that $\sigma_1(n) \geq \alpha$. The Poincaré map writes:

$$\sigma_1(n+1) = \begin{cases} \sigma_1(n) & \alpha < \sigma_1(n) < 1 \\ -\alpha\sigma_1(n) + (1+\alpha) & 1 \leq \sigma_1(n) \leq \frac{1}{\alpha} \\ \alpha^2\sigma_1(n) & \sigma_1(n) > \frac{1}{\alpha}. \end{cases} \tag{6.3}$$

We see (Fig.6.1) that there is a line of marginally stable fixed points $\sigma_1^* \in [\alpha, 1)$, set by the intersection of the map with the bisector. We reported an example of a possible evolution starting from a random value (the blue point) $\sigma_1(n) > 1$. Through the map we may see that after the $(n+1)^{th}$ toppling of 2 $\sigma_1(n+1) < 1$ (the red point). Once it is in this region it will have always the same stress value after every toppling of 2. These fixed points are periodic states with period $1-\alpha$ and σ_1 e σ_2 take turns to topple and the toppling of one site will not trigger the toppling of another ($\sigma_1^* < 1$). The only point of interest would be $\sigma_1^* = 1$, but it is not an attractor of the dynamics.

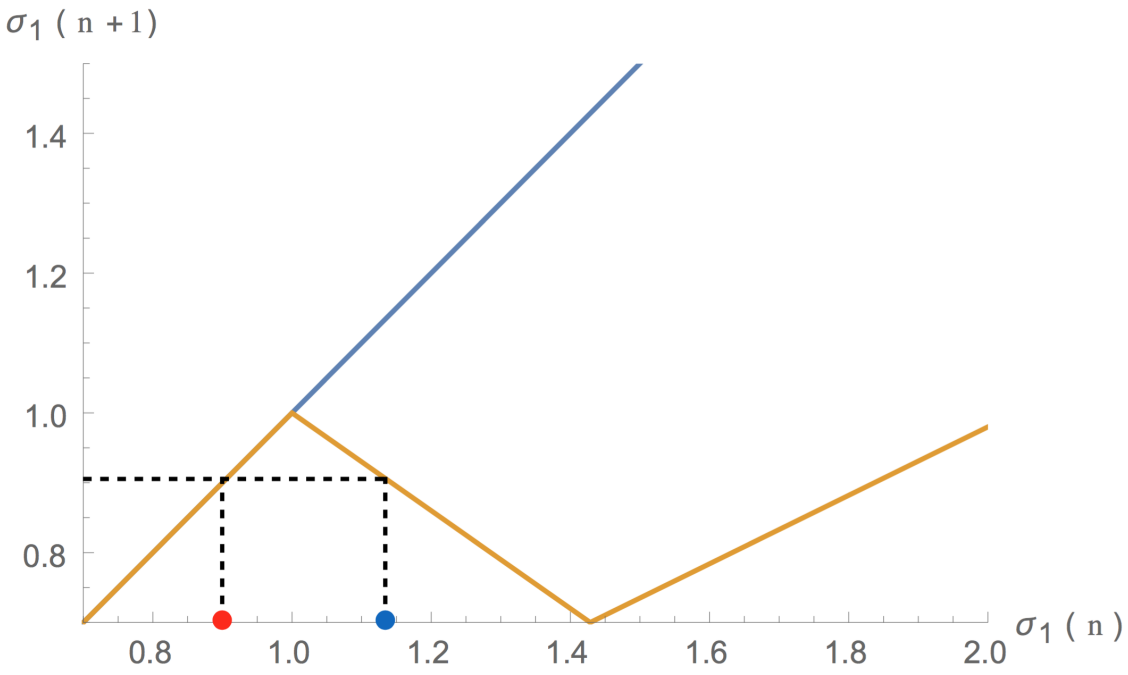

Figure 6.1: Poincaré map in the fixed jump model, for $\alpha = 0.7$ (in blue we report the bisector as a reference for the fixed points). We can see marginal stability for $\sigma_i \in [\alpha, 1)$. In this interval the solution is periodic but there is no synchronization. Each avalanche has size 1. We reported an example of the evolution of σ_1 from a random initial value (the blue point).

6.3 Tang and Middleton: inhomogeneities and synchronization

Tang and Middleton [11] suggested that the introduction of some inhomogeneities in this simple model can induce a phase-locked or synchronized state, where the second oscillator toppling is triggered by the first one's.

For example, if we drive the first oscillator with drive rate 1, and the second one with a sightly slower drive rate $(1 + \epsilon)^{-1}$, we obtain the following Poincaré

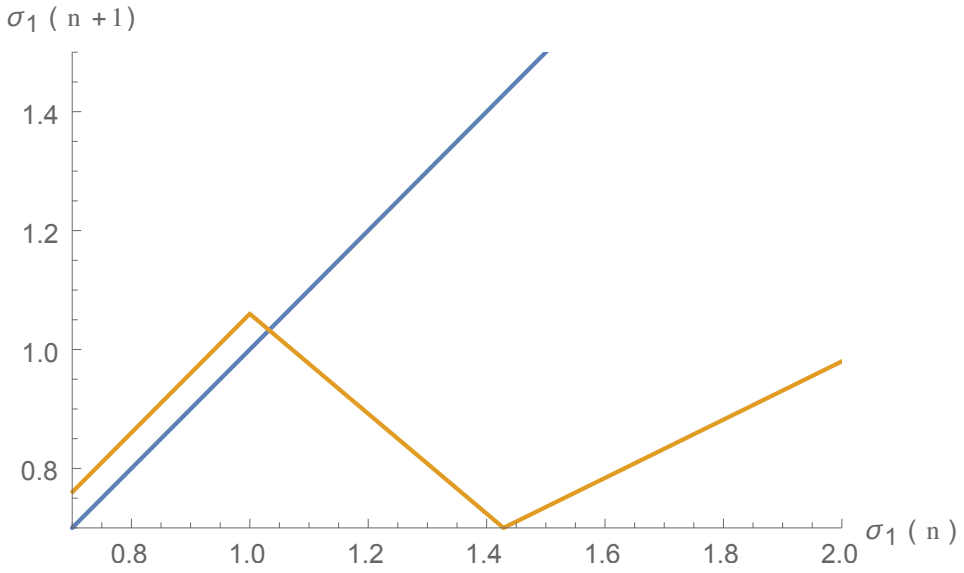

Figure 6.2: Poincaré map in the perturbed fixed jump model, for $\alpha = 0.7$ and $\epsilon = 0.2$. Here we find a single fixed point $\sigma_1^* > 1$. When we arrive here, the system is synchronized: the slow oscillator σ_2 triggers an avalanche of size 2.

map:

$$\sigma_1(n+1) = \begin{cases} \sigma_1(n) + \epsilon(1-\alpha) & \alpha \leq \sigma_1(n) < 1 \\ 1 + \alpha + \epsilon - \alpha(1+\epsilon)\sigma_1(n) & 1 \leq \sigma_1(n) < \frac{1}{\alpha} \\ \alpha^2 \sigma_1(n) & \sigma_1(n) \geq \frac{1}{\alpha}. \end{cases} \tag{6.4}$$

As it is shown in Fig.6.2, this map has only one fixed point:

$$\sigma_1^* = 1 + \epsilon \frac{1-\alpha}{1+\alpha},$$

which corresponds to the synchronized state: the toppling of σ_2 will cause the toppling of σ_1 ($\sigma_1^* > 1$). Note that this map is only ϵ away from the unperturbed one, meaning that the locking is quite weak.

This argument was introduced by Middleton and Tang. Their claim was that the inhomogeneities introduced by open boundary conditions of the system can be responsible for the partial synchronization of the system.

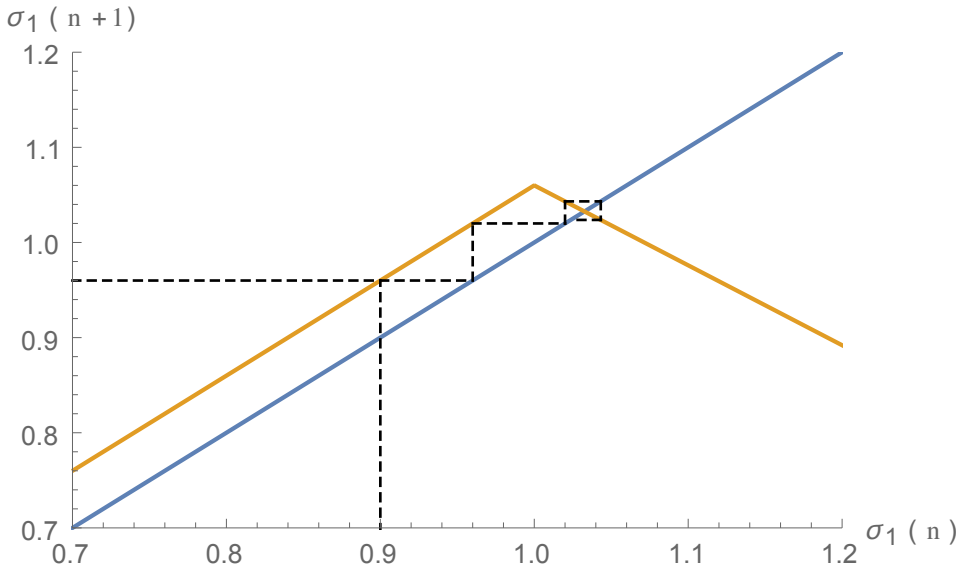

Figure 6.3: Poincaré map in the perturbed fixed jump model: behavior of the attractor

6.4 Relaxation and partial synchronization

Now we introduce a third step in the dynamics of the two oscillator system, the relaxation. This acts on a timescale in between of the two previous regimes, and changes the dynamics in the following way:

- **Drive**:

$$\sigma_i \to \sigma_i + \delta_{\min}, \quad \text{where}$$
$$\delta_{\min} = \min\left(1-\sigma_1, 1-\sigma_2\right)$$

- **Avalanche**: the value σ_i of the oscillator above threshold drops of an amount $(k_2+k_1+k_0)z$ this time, giving to the oscillator a pulse $(k_1+k_2)z$, according to the rules:

$$\sigma_i \quad \to \quad \sigma_i - (k_2+k_1+k_0)z \tag{6.5}$$
$$\sigma_{j\neq i} \quad \to \quad \sigma_j + (k_1+k_2)z \tag{6.6}$$

  where k_2, k_0 and k_1 are positive constants.

- **Relaxation**: After the avalanche is over, the system relaxes:

$$\begin{aligned} \sigma_i &\rightarrow \sigma_i + k_2 z \qquad (6.7) \\ \sigma_{j\neq i} &\rightarrow \sigma_j - k_2 z \qquad (6.8) \end{aligned}$$

In the following we will discuss the jump to zero case, which corresponds to $z = \sigma_i$, $(k_1 + k_0 + k_2)z = \sigma_i + \epsilon$ and $k_1 = \alpha < 1$, where $\epsilon = k_2 z$ is our new perturbation. The randomness is provided by the initial condition only.

The dynamics rules, in term of the parameters α and ϵ, are:

- Drive:

$$\begin{aligned} &\sigma_i \rightarrow \sigma_i + \delta_{\min}, \quad \text{where} \\ &\delta_{\min} = \min\left(1 - \sigma_1, 1 - \sigma_2\right) \end{aligned}$$

- Avalanche:

$$\begin{aligned} \sigma_i &\rightarrow -\epsilon \\ \sigma_{j\neq i} &\rightarrow \sigma_j + \alpha\sigma_i + \epsilon \end{aligned}$$

- Relaxation:

$$\begin{aligned} \sigma_i &\rightarrow \sigma_i + \epsilon \\ \sigma_{j\neq i} &\rightarrow \sigma_j - \epsilon \end{aligned}$$

We calculated the Poincaré map of such a system for the fixed jump case, obtaining:

$$\sigma_1(n+1) = \begin{cases} -\alpha\sigma_1(n) + \alpha(1 + \alpha + 2\epsilon) & \alpha \leq \sigma_1(n) \leq \alpha + 2\epsilon \\ \sigma_1(n) & \alpha + 2\epsilon < \sigma_1(n) < 1 \\ -\alpha\sigma_1(n) + (1 + \alpha + 2\epsilon) & 1 \leq \sigma_1(n) \leq \frac{1}{\alpha} \\ \alpha^2\sigma_1(n) & \sigma_1(n) > \frac{1}{\alpha}. \end{cases} \qquad (6.9)$$

In Fig.6.4 we can see a realization of it for a particular choice of the parameters.

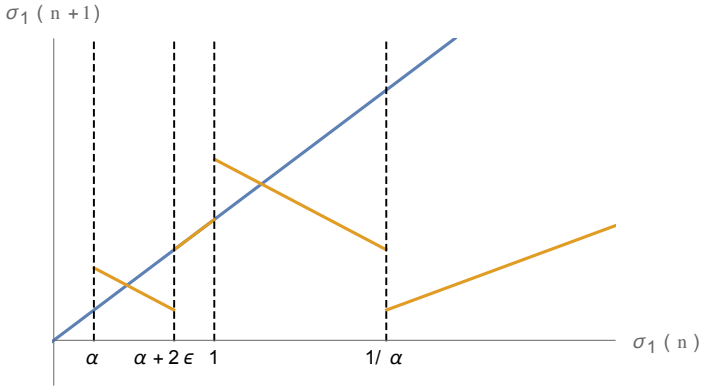

Figure 6.4: Poincaré map in the relaxed fixed jump model, for $\alpha = 0.7$ and $\epsilon = 0.1$ (in blue we report the bisector as a reference for the fixed points).

This map presents a segment of marginally stable fixed point for $\alpha + 2\epsilon < \sigma_1(n) < 1$, which is only present when:

$$\epsilon < \frac{1-\alpha}{2} = f(\alpha);$$

and two non-trivial fixed points:

$$\begin{cases} \sigma_1^* = \alpha + \frac{2\alpha\epsilon}{\alpha+1} & \alpha \leq \sigma_1(n) \leq \alpha + 2\epsilon \\ \sigma_1^* = 1 + \frac{2\epsilon}{\alpha+1} & 1 \leq \sigma_1(n) \leq \frac{1}{\alpha} \end{cases} \tag{6.10}$$

The second point is valid only for

$$\epsilon < \frac{1-\alpha^2}{2\alpha} = g(\alpha),$$

but since $f(\alpha) < g(\alpha) \quad \forall\alpha$, the first condition is sufficient for its existence. This is the one of interest since it is $\sigma_1^* > 1$.

All these considerations have led us to consider three different regimes for ϵ:

- $\epsilon < (1-\alpha)/2$;

- $(1-\alpha)/2 < \epsilon < (1-\alpha^2)/2\alpha$;

- $\epsilon > (1-\alpha^2)/2\alpha$

In Fig.6.5 we can see how the map changes in these three cases, and in the following we will study, for all the cases, the fixed points and the dynamics they suggest more in detail.

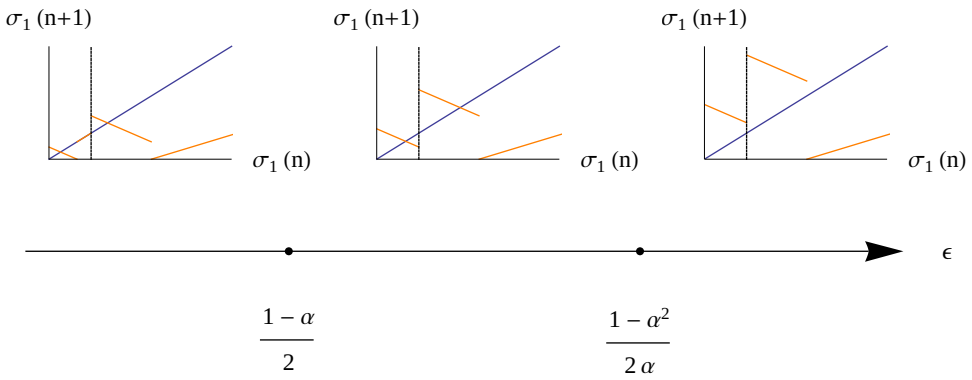

Figure 6.5: Poincaré map in the relaxed fixed jump model, for $\alpha = 0.7$, for the three different regimes. We report, as a reference, the bisector (blue line) and $\sigma_1(n) = 1$ (black dashed line).

6.4.1 Partial Synchronization: $\epsilon < (1-\alpha)/2$

Under this condition, the map is exactly the one we just described in Eq.6.9. As it is suggested by Fig.6.4, this map, unlike the previous case, has an hybrid behaviour:

- In the intervals:

$$\alpha < \sigma_1(n) < \alpha + 2\epsilon \quad \text{and} \quad \frac{1}{\alpha} < \sigma_1(n) < \frac{1}{\alpha} + \frac{2\epsilon}{\alpha^2}$$

  $\sigma_1(n+1)$ tends to be attracted by the first fixed point, even for $\sigma_1(n) > 1$, leading the system to a situation in which the first oscillator will never follow the second one during an avalanche (see Fig.6.6);

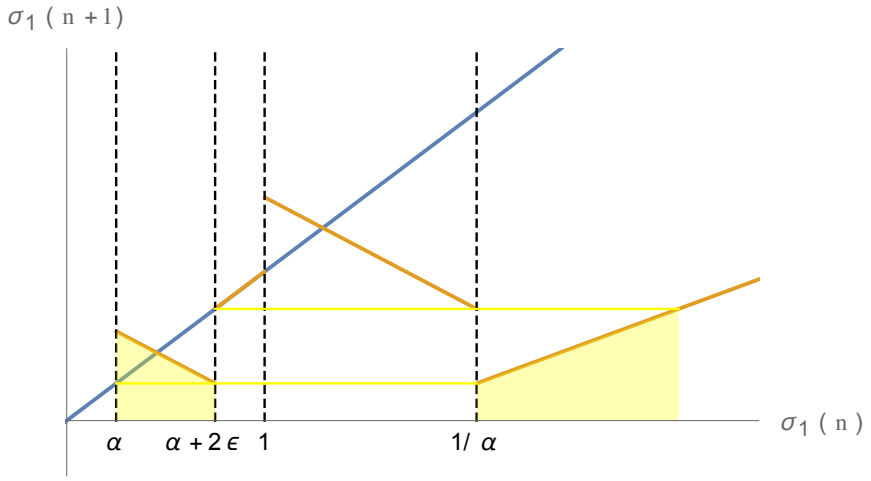

Figure 6.6: Poincaré map in the relaxed fixed jump model, for $\alpha = 0.7$ and $\epsilon = 0.1$: in yellow we can see the $\sigma_1(n)$ values for which the first oscillator tends to go towards the first fixed point. Since this point is $\sigma_1^* < 1$, the avalanche here has size 1.

- in the intervals:

$$\alpha + 2\epsilon < \sigma_1(n) < 1, \quad 1 + \frac{2\epsilon}{\alpha} < \sigma_1(n) < \frac{1}{\alpha} \quad \text{and} \quad \frac{1}{\alpha} + \frac{2\epsilon}{\alpha^2} < \sigma_1(n) < \frac{1}{\alpha^2}$$

  the system tends to go in the marginally stable points and then it is stuck there in a periodic state (see Fig.6.7);

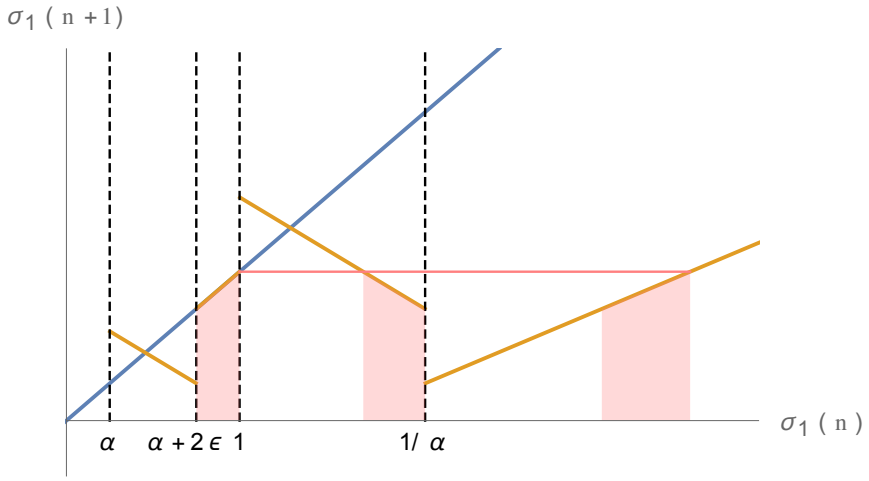

Figure 6.7: Poincaré map in the relaxed fixed jump model, for $\alpha = 0.7$ and $\epsilon = 0.1$: in pink we can see the $\sigma_1(n)$ values for which the first oscillator goes into the set of periodic states $\sigma_1(n+1) = \sigma_1(n) < 1$, in which it remains. Again, we have avalanches of size 1.

- in the intervals

$$1 < \sigma_1(n) < 1 + \frac{2\epsilon}{\alpha} \quad \text{and} \quad \frac{1}{\alpha^2} < \sigma_1(n) < \frac{1}{\alpha^2} + \frac{2\epsilon}{\alpha^3}$$

the system is attracted now by a single fixed point (see Fig.6.8):

$$\sigma_1^* = 1 + \frac{2\epsilon}{\alpha + 1} > 1;$$

here the system is synchronized, meaning that a toppling of the second oscillator will always trigger a toppling of the first one.

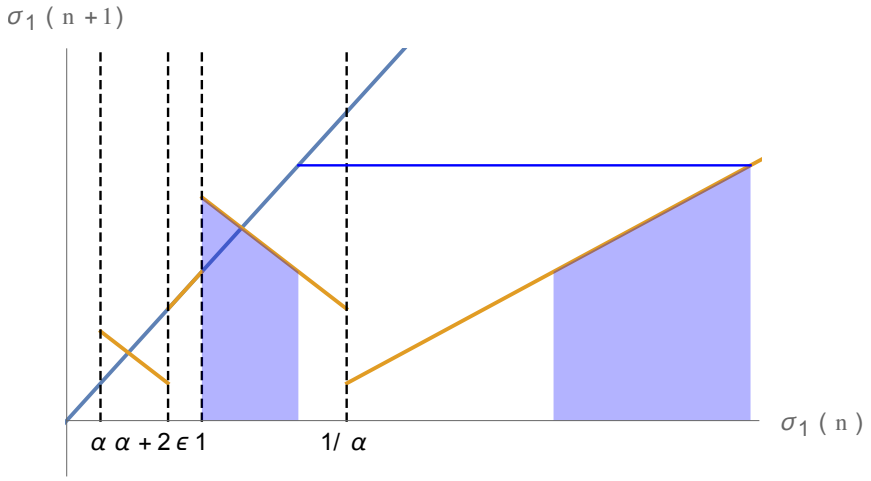

.

Figure 6.8: Poincaré map in the relaxed fixed jump model, for $\alpha = 0.7$ and $\epsilon = 0.1$: in blue we can see the $\sigma_1(n)$ values for which the first oscillator is attracted by the fixed point $\sigma_1^* > 1$. Here we have avalanches of size 2, triggered by σ_2

6.4.2 Synchronization: $(1-\alpha)/2 < \epsilon < (1-\alpha^2)/2\alpha$

The segment of marginally stable points disappears and the only fixed points of the system are the two attractors found before. The map reads:

$$\sigma_1(n+1) = \begin{cases} -\alpha\sigma_1(n) + \alpha(1+\alpha+2\epsilon) & \alpha \leq \sigma_1(n) \leq 1 \\ -\alpha\sigma_1(n) + (1+\alpha+2\epsilon) & 1 \leq \sigma_1(n) \leq \frac{1}{\alpha} \\ \alpha^2\sigma_1(n) & \sigma_1(n) > \frac{1}{\alpha}. \end{cases} \tag{6.11}$$

. We still have to distinguish the $\sigma_1(n)$ values for which the system is attracted by the two fixed points (see Fig.6.9):

- $\alpha < \sigma_1(n) < 1$ and $1/\alpha < \sigma_1(n) < 1/\alpha^2$:
  with the starting point belonging to these intervals, the system is attracted by the fixed point $\sigma_1^* < 1$, leading to avalanches of size 1;

- $1 < \sigma_1(n) < 1/\alpha$ and $\sigma_1(n) > 1/\alpha^2$:
  with the starting point belonging to these intervals, the system is attracted

by the fixed point $\sigma_1^* > 1$, leading to synchronized avalanches of size 2;

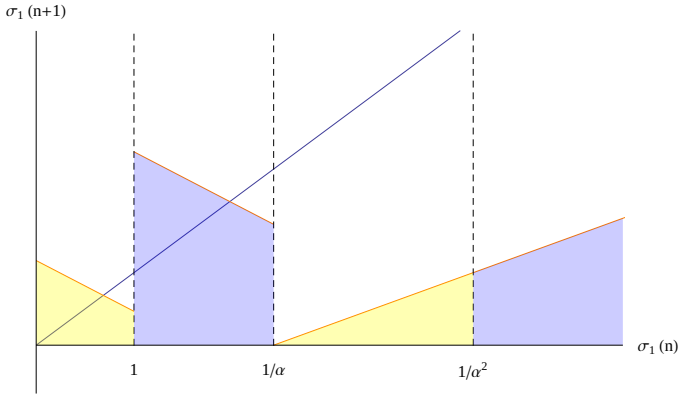

Figure 6.9: Poincaré map in the relaxed fixed jump model , for $\alpha = 0.7$ and $\epsilon = 0.25$: 1) in blue we marked the $\sigma_1(n)$ values for which the first oscillator is attracted by the fixed point $\sigma_1^* > 1$. Here we have avalanches of size 2, triggered by σ_2; 2) in yellow we marked the $\sigma_1(n)$ values for which the first oscillator is attracted by the fixed point $\sigma_1^* < 1$. Here we have avalanches of size 1.

6.4.3 Periodicity: $\epsilon > (1 - \alpha^2)/2\alpha$

In this case the map is the same of the previous case, but we don't have anymore fixed points. The behavior, though, seems to be periodic in visiting the three different domains of the map. In Fig.6.10 we report an example of such a trajectory. If we start with $\sigma_1(n) < 1$, we have:

- $1 < \sigma_1(n+1) < 1/\alpha$
- $\sigma_1(n+2) > 1/\alpha$
- $\sigma_1(n+3) < 1$

After that, this cycle repeat itself, visiting again the three domains in the same order. After a transient, the system goes into the limit cycle (see Fig.6.10), where it stays, and here we have:

$$\sigma_1(n+3) = \sigma_1(n).$$

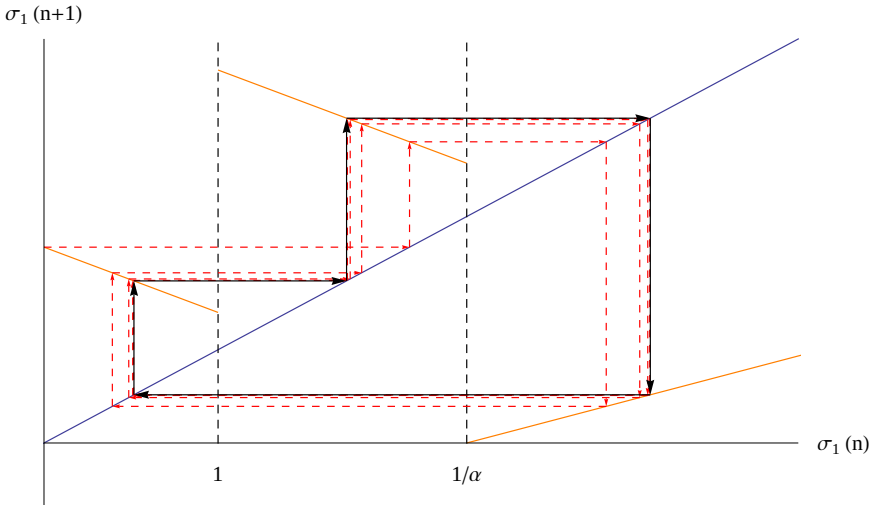

Figure 6.10: Poincare map in the relaxed fixed jump model, for $\alpha = 0.7$, $\epsilon = 0.45$. The red dashed line represents a typical evolution of the system in this case; despite the fact that there is not a fixed point, the system is attracted by the limit cycle marked in black. The avalanches here have size 3.

In order to find the points among which the system oscillates, once it arrives in the limit cycle, we calculated the following map :

$$\sigma_1(n+3) = \begin{cases} \alpha^4\sigma_1(n) + \alpha^2(1-\alpha^2)(1+\alpha+2\epsilon) & \alpha \leq \sigma_1(n) \leq 1 \\ \alpha^4\sigma_1(n) + \alpha(1-\alpha^2)(1+\alpha+2\epsilon) & 1 \leq \sigma_1(n) \leq \frac{1}{\alpha} \\ \alpha^4\sigma_1(n) + (1-\alpha^2)(1+\alpha+2\epsilon) & \sigma_1(n) > \frac{1}{\alpha}. \end{cases} \tag{6.12}$$

. In Fig.6.11 we report an example of this map.

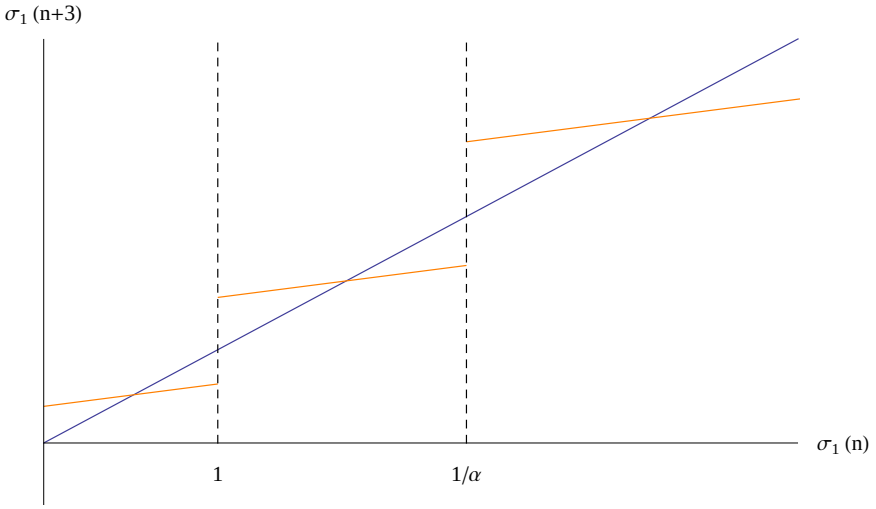

Figure 6.11: A realization of the map $\sigma_1(n+3) = f(\sigma_1(n))$, for for $\alpha = 0.7$, $\epsilon = 0.45$.

The three fixed points of this map, which corresponds to the vertexes of the limit cycle, are:

$$\sigma_1^*(n) = \begin{cases} \alpha^2 \frac{1+\alpha+2\epsilon}{1+\alpha^2} & \alpha \leq \sigma_1(n) \leq 1 \\ \alpha \frac{1+\alpha+2\epsilon}{1+\alpha^2} & 1 \leq \sigma_1(n) \leq \frac{1}{\alpha} \\ \frac{1+\alpha+2\epsilon}{1+\alpha^2} & \sigma_1(n) > \frac{1}{\alpha}. \end{cases} \tag{6.13}$$

.

Conclusions

Spring-block models are the most simple description of a seismic fault reproducing at qualitative level experimental observations as the Gutenberg-Richter law [3].

In the Burridge-Knopoff model [1] the fault is represented as an array of blocks on a rough surface, elastically coupled with a driving plate and with each other. The blocks are uniformly driven by the plate until the stress exercised on one of them overcomes the static friction. The block slides and its stress topples to zero, being redistributed to the neighbors through the elastic coupling. The redistribution may induce some other block to slide, and so on, leading to an avalanche of topplings that ends when all the blocks' stress is again under the threshold set by the static friction. This model induces two time scales in the dynamics, the first one of the driving τ_D and the second one of the avalanches τ_0, instantaneous if compared to the drive.

In the cellular automata version, the so-called OFC model [2], randomness is present only in the initial condition and avalanche sizes follow a power law distribution. OFC is one of a class of systems that displays self-organized criticality (SOC) [55]. In these systems we find a critical behavior without any tuning of external parameters. Most of these systems, though, presents critical behavior only when there is no dissipation in the redistribution process to the neighbors. On the other hand, the OFC model presents a power law behavior also in the non conservative case, with an exponent depending on the dissipation parameter α.

The OFC model can be mapped in the evolution of a driven elastic interface in a disordered medium (OFC* model) after adding annealed randomness in the level of friction instability. In this case the avalanche size distribution is still a power law but with a stable exponent independent of the dissipation parameter, which influences only the cut-off of the distribution.

In this Thesis we studied the mechanism responsible for the observed differences between the pure and the random OFC model, focusing on the role of synchronization leading to quasi-periodic behavior.

We studied a fully connected model of four different variants of the OFC dynamics:

1) the stress σ_i of the unstable site drops to zero, giving a pulse $\alpha\sigma_i$ to all the sites (OFC mean field);

2) the stress σ_i of the unstable site drops of a fixed amount k, giving a pulse αk to all the sites (generalized BTW mean field);

3) the stress σ_i of the unstable site drops of a random amount x, giving a pulse αx to all the sites (OFC* mean field);

4) the stress σ_i of the unstable site drops of a random amount x, giving a pulse αx to all the sites; moreover we introduced also annealed disorder in the thresholds (modified OFC* mean field).

In the last three cases we verify a critical behavior in the limit $\alpha \to \alpha_c$.

For the first two cases we were able to follow the evolution of the stress gaps, in order to address the role of synchronization in the critical behavior of the system. In the case of the OFC model the dynamics destroys the correlations among sites leading, after a transient, to a regime of avalanches of size 1, while in 2-dim a partial synchronization exists, due to inhomogeneities propagating from the boundaries. In the second model, conversely, the system converges to a regime of periodic avalanches, since the dynamics does not affect the stress gaps. Actually, it is possible to retrieve the avalanche size distribution from a static evaluation of the stress gaps, and the results are the same as the ones obtained from the dynamics. We obtained for the size distribution a power law behavior with an exponent $\tau \simeq 1.5$ and with an exponential cut-off $s_m \propto (\alpha_c - \alpha)^{-2}$, where $\alpha_c = 1/N$ is the conservative limit. The last two cases gave identical outcomes, indicating that the

addition of more randomness in the system does not influence the dynamics. They both present a non periodic behavior and the same avalanche size distribution, even the cut-off are the same, unlike the 2-dim case where the randomness in thresholds changes their numerical value. The avalanche size distribution is the same as in the generalized BTW MF, with $\tau \simeq 1.5$ as well, while in 2-dim the exponent of the distribution of the generalized BTW and the one of the OFC* have different values. The cut-off of this distribution, in the respect of model 2), are slightly different, but their dependence on the distance to the conservative limit is the same. In Table 6.1 we report a summary of the results of the models we studied in 2-dim and in mean field to facilitate a confrontation.

2 dim	**OFC**	**(g) BTW**	**OFC***	**(m) OFC***
$P(s)$	$s^{-\tau}$	$s^{-\tau}\exp(-(s/s_m)^{1.3})$	$s^{-\tau}\exp(-s/s_m)$	$s^{-\tau}\exp(-s/s_m)$
τ	$\tau(\alpha)$	$\tau \simeq 1$	$\tau \simeq 1.3$	$\tau \simeq 1.3$
s_m	$s_m(N)$	$(\alpha_c - \alpha)^{-1}$	$(\alpha_c - \alpha)^{-1.4}$	$(\alpha_c - \alpha)^{-1.4}$

M. F.	**OFC**	**(g) BTW**	**OFC***	**(m) OFC***
$P(s)$	$\delta(s-1)$	$s^{-\tau}\exp(-(s/s_m))$	$s^{-\tau}\exp(-s/s_m)$	$s^{-\tau}\exp(-s/s_m)$
τ		$\tau \simeq 1.5$	$\tau \simeq 1.5$	$\tau \simeq 1.5$
s_m		$(\alpha_c - \alpha)^{-2}$	$(\alpha_c - \alpha)^{-2}$	$(\alpha_c - \alpha)^{-2}$

Table 6.1: Numerical results of the avalanche size distribution in 2 dim and in Mean Field for the four models we considered

It is possible to understand the consistency in mean field of model 2) and 3) mapping them onto the problem of the first passage of a random walk. In Fig.5.5 and Fig.5.9 we reported a schematic example of the two cases. While in the first case the randomness it is just in the initial condition of the stress (and then in the variable $S_n = \sigma_1 - \sigma_n$), in the second one there is also randomness in the killing wall, since the killing wall represents the locking condition, that depends on the pulse q that a site gives when it becomes unstable. In both cases though we have the same synchronization mechanism.

In finite dimension, as we mentioned before, we observe a different exponent for the two models but in both cases it is stable with dissipation. Since the introduction of randomness does not change the statistics in mean field, we observe that the synchronization mechanism is a possible good candidate to justify the stability of the exponent τ with dissipation, while randomness is related to the

presence of a not periodic behavior.

The similarity of the mean field behavior of model 2), 3) and 4) suggests that their finite dimension behavior can be obtained via a perturbative expansion around mean-field theory. The situation is totally different for model 1), i.e. the standard OFC model, which presents an annealing of synchronization in mean field.

An interesting variation of the OFC* model is the so-called OFCR model [7]. In order to consider the viscosity effect, a relaxation mechanism is introduced, on a time scale τ_R that is in the middle between the time scales of the drive and the avalanche: $\tau_0 \ll \tau_R \ll \tau_D$. The effect of this mechanism is to smoothen the stress field. The two main consequences of the relaxation are: 1) the presence of the aftershocks, that corresponds to the events triggered by the relaxation; 2) an exponent $\tau \simeq 1.7$ for the avalanche size distribution, in very good agreement with the Gutenberg Richter law.

In order to study the effect of the relaxation on the synchronization of the system, we analytically investigated a simple 2-blocks model with fixed thresholds. We evaluated the Poincaré map of the process and we discovered three regimes of synchronization, as the relaxation parameter ϵ grows with the dissipation α:

- Partial Synchronization ($\epsilon < (1-\alpha)/2$): we have 2 fixed points $\sigma_1* < 1$ and $\sigma_1* > 1$ and a segment of metastable points on the bisector all less than 1;
- Synchronization ($(1-\alpha)/2 < \epsilon < (1-\alpha)^2/2\alpha$): we have 2 fixed points $\sigma_1* < 1$ and $\sigma_1* > 1$;
- Periodicity ($\epsilon > (1-\alpha)^2/2\alpha$): there are not fixed points but the system is attracted to a limit cycle that corresponds to a periodic state.

The results are reported in Fig.6.5.

Future developments of this work can be related to the study of the transition of these models from mean field to finite connectivity in term of synchronization. This would give us a better understanding of the relationships of our results with the 2-dim models. Another progress would be to find a way to study the effect of relaxation on synchronization in the case of a random jump, which would corresponds to the proper OFCR model.

Bibliography

[1] R. Burridge, L. Knopoff, *Model and theoretical seismicity*, Bull. Seismol. Soc. Am. 57 (1967), 341-371.

[2] Z. Olami, H. J. S. Feder, K. Christensen, *Self-organized criticality in a continuous, nonconservative cellular automaton modeling earthquakes*, Phys. Rev. Lett. 68 (1992), 1244-1247.

[3] B. Gutenberg, C. Richter, *Frequency of earthquakes in California*, Bulletin of the Seismological Society of America 34 (1944), 185188.

[4] P. Bak, C. Tang, K. Wiesenfeld, *Self-organized criticality: An explanation of the 1/f noise*, Phys. Rev. Lett. 59(4) (1987), 381.

[5] H.J. Jensen, *Self-Organized Criticality: Emergent Complex Behavior in Physical and Biological Systems*, (Cambridge Lecture Notes in Physics, 1998)

[6] P. Ghaffari, S. Lise and H. J. Jensen, *Non conservative sandpile models*, Phys. Rev. E 56.6 (1997), 6702.

[7] E. A. Jagla, *Realistic spatial and temporal earthquake distributions in a modified Olami-Feder-Christensen model*, Phys. Rev. E 81 (2010), 046117.

[8] E. E. Ferrero, S. Bustingorry, A. B. Kolton and A. Rosso,*Numerical approaches on driven elastic interfaces in random media*, Comptes Rendus Physique, 14(8) (2013), 641-650.

[9] F. Omori, *On the aftershocks of earthquakes*, Journal of the College of Science Imperial University of Tokyo 7 (1894), 111-200.

[10] E. A. Jagla, F. P. Landes, A. Rosso, *Viscoelastic effects in avalanche dynamics: A key to earthquake statistics*, Phys. Rev. Lett. 112 (2014), 174301.

[11] A. Middleton, C. Tang, *Self-organized criticality in nonconserved systems*, Phys. Rev. Lett. 74 (1995), 742-745.

[12] R. Roy and K. Thornburg, *Experimental synchronization of chaotic lasers*Phys. Rev. Lett. 72 (1994), 2009.

[13] D. Fisher, *Sliding charge-density waves as a dynamic critical phenomenon*, Physical Review B 31.3 (1985), 1396.

[14] S. Strogatz, C. Marcus, R. Westervelt, and R. Mirollo, *Collective dynamics of coupled oscillators with random pinning*, Physica D 36 (1989), 23-50.

[15] K. Y. Tsang et al.*Reversibility and noise sensitivity of Josephson arrays*, Physical review letters 66.8 (1991), 1094.

[16] F. E. Hanson et al., *Synchrony and flash entrainment in a New Guinea firefly*, Science 174.4005 (1971), 161-164.

[17] E. Sismondo, *Synchronous, alternating, and phase-locked stridulation by a tropical katydid*, Science 249.4964 (1990), 55-59.

[18] R. E. Mirollo, S. H. Strogatz, *Synchronization of pulse-coupled biological oscillators*, SIAM Journal on Applied Mathematics 50.6 (1990), 1645-1662.

[19] C. Liu et al., *Cellular construction of a circadian clock: period determination in the suprachiasmatic nuclei*, Cell 91.6 (1997), 855-860.

[20] , J. Aldridge, E. K. Pye, *Cell density dependence of oscillatory metabolism*, Nature 259.5545 (1976), 670-671.

[21] G. Mercalli, *Improved Mercalli Scale*, Boll. Soc. Sismologica Italiana (8) (1902), 184-191.

[22] C. F. Richter, *An instrumental earthquake magnitude scale*, Bulletin of the Seismological Society of America 25.1 (1935), 1-32.

[23] H. Kanamori, *The energy release in great earthquakes*, Journal of Geophysical Research 82 (20) (1977), 2981-2987.

[24] D. L. Wells, K. J. Coppersmith, *New empirical relationships among magnitude, rupture length, rupture width, rupture area, and surface displacement*, Bulletin of the Seismological Society of America 84 (4) (1994), 974-1002.

[25] K. Wadati, *On the frequency distribution of earthquakes*, Journal Metereological Society Japan 10 (1932), 559-568.

[26] P. A. Rydelek, I. S. Sacks, *Testing the completeness of earthquake catalogs and the hypothesis of self-similarity*, Nature 337 (1989), 251-253.

[27] K. Hutton, J. Woessner, E. Hauksson, *Earthquake Monitoring in Southern California for Seventy-Seven Years (1932-2008)*,Bulletin of the Seismological Society of America (April 2010), vol. 100 no. 2, 423-446.

[28] S. Wiemer, M. Wyss, *Mapping spatial variability of the frequency-magnitude distribution of earthquakes*, Adv. Geophys. 45 (2002), 259-302.

[29] D. Amorse, J. R. Grasso, P. A. Rydelek, *On varying b-values with depth: results from computer-intensive tests for southern california*, Geophysical Journal International 180 (1) (2010), 347-360.

[30] D. Schorlemmer, S. Wiemer, M. Wyss, *Variations in earthquake-size distribution across different stress regimes*, Nature 437.7058 (2005), 539-542.

[31] R. H. Sibson, *Frictional constraints on thrust, wrench and normal faults*, Nature 249 (1974), 542-544.

[32] ,C. Godano, E. Lippiello, L. de Arcangelis, *Variability of the b value in the gutenberg richter distribution*, Geophysical Journal International 199 (3) (2014), 1765-1771.

[33] T. Utsu, *Statistical features of seismicity*, In Lee, W. H. K. (ed.), International Handbook of Earthquake and Engineering Seismology, Part A, San Diego: Academic (2002), pp. 719-732.

[34] T. Utsu, *A statistical study of the occurrence of aftershocks*, Geophysical Magazine 30 (1961), 521-605.

[35] P. A. Reasenberg, L. M. Jones, *Earthquake hazard after a mainshock in california*, Science 243 (4895) (1989), 1173-1176.

[36] M. Bath, *Lateral inhomogeneities in the upper mantle*, Tectonophysics 2 (1965), 483-51.

[37] E. Lippiello, L. de Arcangelis, C. Godano, *Role of static stress diffusion in the spatiotemporal organization of aftershocks*, Phys. Rev. Lett. 103 (2009), 038501.

[38] Y. Y. Kagan, *Short-term properties of earthquake catalogs and models of earthquake source*, Bulletin of the Seismological Society of America 94 (4) (2004), 1207-1228.

[39] A. Helmstetter, Y. Y. Kagan, D. D. Jackson, *Importance of small earthquakes for stress transfers and earthquake triggering*, Journal of Geophysical Research: Solid Earth 110 (B5) (2005), B05S08.

[40] E. Lippiello, M. Bottiglieri, C. Godano, L. de Arcangelis, *Dynamical scaling and generalized Omori law*, Geophysical Research Letters 34, (2007) 23.

[41] C. Narteau, S. Byrdina, P. Shebalin, D. Schorlemmer, *Common dependence on stress for the two fundamental laws of statistical seismology*, Nature 462 (2009), 642-645.

[42] A. Helmstetter, *Is earthquake triggering driven by small earthquakes?*, Phys. Rev. Lett. 91 (2003), 058501.

[43] M. Baiesi, M. Paczuski, *Scale-free networks of earthquakes and aftershocks*, Phys. Rev. E 69 (2004), 066106.

[44] Y. Ogata, J. Zhuang, *Space?time ETAS models and an improved extension*, Tectonophysics 413.1 (2006), 13-23.

[45] H. Kanamori, *The alaska earthquake of 1964: Radiation of long-period surface waves and source mechanism*, Journal of Geophysical Research 75 (26) (1970), 5029-5040.

[46] M. Baiesi, M. Paczuski, *Complex networks of earthquakes and aftershocks*, Nonlinear Processes in Geophysics 12 (1) (2005), 1-11.

[47] K. R. Felzer, E. E. Brodsky, *Decay of aftershock density with distance indicates triggering by dynamic stress*, Nature 441 (2006), 735-738.

[48] D. P. Hill et al., *Seismicity remotely triggered by the magnitude 7.3 Landers, California, earthquake*, Science 260.5114 (1993), 1617-1624.

[49] S. Hergarten, *Self organized criticality in earth systems*, Springer (2002), 130-133.

[50] J. M. Carlson, J. S. Langer, *Properties of earthquakes generated by fault dynamics*, Phys. Rev. Lett. 62 (1989), 2632-2635.

[51] T. Mori and H. Kawamura, *Simulation study of the two-dimensional Burridge-Knopoff model of earthquakes*, Journal of Geophysical Research: Solid Earth 113 (2008), B6.

[52] T. Mori, H. Kawamura, *Simulation study of earthquakes based on the two-dimensional Burridge-Knopoff model with long-range interactions*, Phys. Rev. E 77 (2008), 051123.

[53] M. de Sousa Vieira, *Self-organized criticality in a deterministic mechanical model*, Phys. Rev. A 46 (1992), 6288.

[54] L. de Arcangelis, C. Godano, J. R. Grasso, and E. Lippiello, *Statistical physics approach to earthquake occurrence and forecasting*, Physics Reports 628, 1 (2016).

[55] P. Bak, C. Tang, *Earthquakes as a self-organized critical phenomenon*, Journal of Geophysical Research: Solid Earth 94 (B11) (1989), 15635-15637.

[56] H. J. S. Feder and J. Feder, *Self-Organized Criticality in a Stick-Slip process*, Phys. Rev. Lett. 66 (1991), 2669-72.

[57] M. Kardar, *Non equilibrium dynamics of interfaces and lines*, Physics Reports 301(13)(1998), 85-112.

[58] T. Hwa, M. Kardar, *Dissipative transport in open systems: An investigation of self-organized criticality*, Phys. Rev. Lett. 62 (1989), 1813-1816.

[59] S. F. Edwards, D. R. Wilkinson, *The surface statistics of a granular aggregate*, Proceedings of the Royal Society of London A: Mathematical, Physical and Engineering Sciences 381 (1780) (1982), 17-31.

[60] B. Alessandro, C. Beatrice, G. Bertotti, A. Montorsi, *Domain wall dynamics and Barkhausen effect in metallic ferromagnetic materials. ii. Experiments*, Journal of Applied Physics 68 (6) (1990), 2908-2915.

[61] F. P. Landes, *Viscoelastic Interfaces Driven in Disordered Media and Applications to Friction*, These de doctorat, Springer (2015)

[62] D. S. Fisher, *Collective transport in random media: from superconductors to earthquakes*, Physics Reports, 301(1-3) (1998), 113-150.

[63] P. Le Doussal, K. J. Wiese, *Size distributions of shocks and static avalanches from the functional renormalization group*, Phys. Rev. E 79 (2009), 051106.

[64] A. Rosso, A. K. Hartmann, W. Krauth, *Depinning of elastic manifolds*, Phys. Rev. E 67 (2003), 021602.

[65] L. E. Aragon, E. A. Jagla, A. Rosso, *Seismic cycles, size of the largest events, and the avalanche size distribution in a model of seismicity*, Phys. Rev. E 85 (2012,) 046112.

[66] S. Zapperi, P. Cizeau, G. Durin and H. Stanley, *Dynamics of a ferromagnetic domain wall: Avalanches, depinning transition, and the Barkhausen e ect.*, Physical Review B, 58(10) (1998), 6353-6366.

[67] P. Le Doussal and K. Wiese, *Driven particle in a random landscape: Disorder correlator, avalanche distribution, and extreme value statistics of records*, Physical Review E, 79(5) (2009), 51105.

[68] S. Majumdar and A. Comtet, *Exact asymptotic results for persistence in the Sinai model with arbitrary drift*, Physical Review E, 66(6) (2002), 061105.

[69] R.E. Mirollo, S. H. Strogatz, *Synchronization of pulse-coupled biological oscillators*, SIAM Journal on Applied Mathematics 50.6 (1990), 1645-1662.

[70] S. Bottani, *Synchronization of integrate and fire oscillators with global coupling*, Phys. Rev. E 54.3 (1996), 2334.

[71] P. Grassberger, *Efficient large-scale simulations of a uniformly driven system*, Phys. Rev. E 49 (1994), 2436

[72] S.M. Ross, *Stochastic processes. Second Edition.*, Wiley (1996).

[73] H. Nakanishi, *Cellular-automaton model of earthquakes with deterministic dynamics*, Phys. Rev. A 41 (1990), 7086-7089.

[74] S. Hainzl, G. Zller, J. Kurths, *Similar power laws for foreshock and aftershock sequences in a spring-block model for earthquakes*, Journal of Geophysical Research: Solid Earth 104 (B4) (1999), 7243-253.

[75] J. Pelletier, *Spring-block models of seismicity: Review and analysis of a structurally heterogeneous model coupled to a viscous asthenosphere*, GeoComplexity and the Physics of Earthquakes (2000), 27-42.

[76] C.Narteau,S.Byrdina,P.Shebalin,D.Schorlemmer, *Common dependence on stress for the twof undamental laws of statistical seismology*, Nature 462 (2009), 642-645.

Acknowledgements

I would like to thank Dr. Eugenio Lippiello for supervising my thesis efficiently and kindly, it was a real pleasure to work with him. I warmly thank Dr. Alberto Rosso, for insightful discussions and for the opportunity to know and appreciate a new challenging work environment, and to the LPTMS, Université Paris Sud, where I felt really welcome and supported. I also have to thank Prof. Massimo Pica Ciamarra, for the precious advices. Thanks to Dr. Francois Landes, whose work was determinant for the development of my thesis. A huge thanks to Dr. Ferdinando Giacco, who gave me a great technical and moral support, and to all the coworkers from University of Campania, who made my days there brighter and happier. Finally, it would be an oversight on my part if I failed to thank my family, my partner and my friends for their incitements and their trust in my capacities. I am a lucky person to have you to back me up.